Remodeling of the Collagen Matrix in Aging Skin Promotes Melanoma Metastasis and Affects Immune Cell Motility

Amanpreet Kaur[1,2,3], Brett L. Ecker[2], Stephen M. Douglass[2], Curtis H. Kugel III[2], Marie R. Webster[2], Filipe V. Almeida[2], Rajasekharan Somasundaram[2], James Hayden[2], Ehsan Ban[3], Hossein Ahmadzadeh[3], Janusz Franco-Barraza[4], Neelima Shah[4], Ian A. Mellis[3], Frederick Keeney[2], Andrew Kossenkov[2], Hsin-Yao Tang[2], Xiangfan Yin[2], Qin Liu[2], Xiaowei Xu[5], Mitchell Fane[2], Patricia Brafford[2], Meenhard Herlyn[2], David W. Speicher[2], Jennifer A. Wargo[6], Michael T. Tetzlaff[6], Lauren E. Haydu[6], Arjun Raj[3], Vivek Shenoy[3], Edna Cukierman[4], and Ashani T. Weeraratna[2]

ABSTRACT

Physical changes in skin are among the most visible signs of aging. We found that young dermal fibroblasts secrete high levels of extracellular matrix (ECM) constituents, including proteoglycans, glycoproteins, and cartilage-linking proteins. The most abundantly secreted was HAPLN1, a hyaluronic and proteoglycan link protein. HAPLN1 was lost in aged fibroblasts, resulting in a more aligned ECM that promoted metastasis of melanoma cells. Reconstituting HAPLN1 inhibited metastasis in an aged microenvironment, in 3-D skin reconstruction models, and *in vivo*. Intriguingly, aged fibroblast-derived matrices had the opposite effect on the migration of T cells, inhibiting their motility. HAPLN1 treatment of aged fibroblasts restored motility of mononuclear immune cells, while impeding that of polymorphonuclear immune cells, which in turn affected regulatory T-cell recruitment. These data suggest that although age-related physical changes in the ECM can promote tumor cell motility, they may adversely affect the motility of some immune cells, resulting in an overall change in the immune microenvironment. Understanding the physical changes in aging skin may provide avenues for more effective therapy for older patients with melanoma.

SIGNIFICANCE: These data shed light on the mechanochemical interactions that occur between aged skin, tumor, and immune cell populations, which may affect tumor metastasis and immune cell infiltration, with implications for the efficacy of current therapies for melanoma.

See related commentary by Marie and Merlino, p. 19.

[1]Department of Biological Sciences, University of the Sciences, Philadelphia, Pennsylvania. [2]The Wistar Institute, Philadelphia, Pennsylvania. [3]School of Engineering and Applied Science, Center for Engineering Mechanobiology, University of Pennsylvania, Philadelphia, Pennsylvania. [4]Cancer Biology Program, Fox Chase Cancer Center, Philadelphia, Pennsylvania. [5]Department of Pathology, University of Pennsylvania, Philadelphia, Pennsylvania. [6]The University of Texas MD Anderson Cancer Center, Houston, Texas.

Note: Supplementary data for this article are available at Cancer Discovery Online (http://cancerdiscovery.aacrjournals.org/).

Corresponding Author: Ashani T. Weeraratna, The Wistar Institute, 3601 Spruce Street, Philadelphia, PA 19104. Phone: 215 495-6937; Fax: 215 495-6938; E-mail: aweeraratna@wistar.org

doi: 10.1158/2159-8290.CD-18-0193

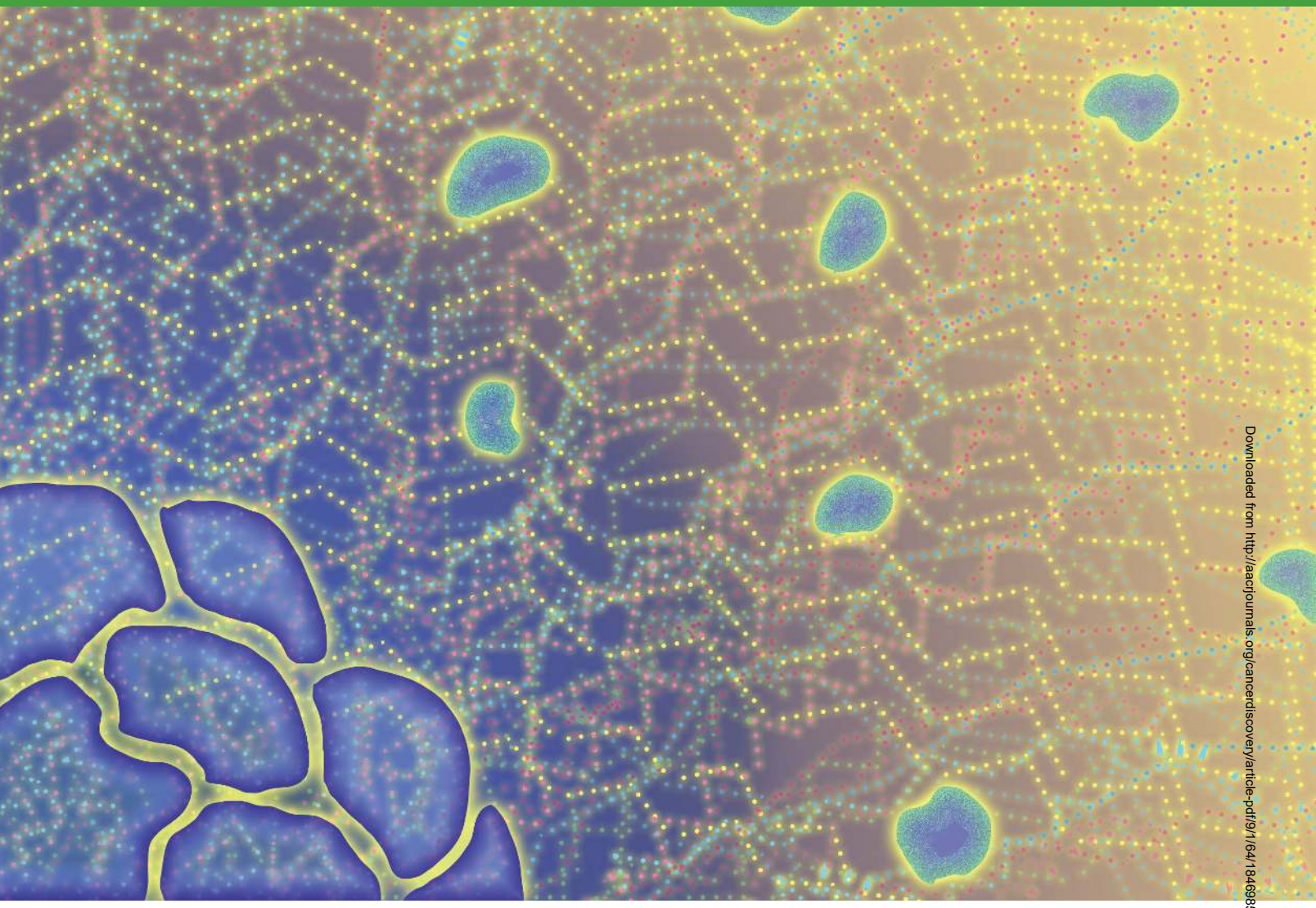

INTRODUCTION

Melanoma, the malignant transformation of epidermal melanocytes, is the leading global cause of skin cancer–related death. Increasing age is a negative prognostic indicator, and elderly patients with melanoma have inferior disease-specific survival even when controlling for primary tumor factors (1). Although age-related differences in tumor molecular pathways and host immune response may partly underlie these findings (2), the influence of age on the architectural changes that may govern immune and tumor cell trafficking through the skin has not been well studied. Previously, we reported that fibroblasts in the aged dermal microenvironment (age >55 years) contribute to melanoma tumor progression by secreting factors that promote metastasis and resistance to targeted therapy (3). In the present study, we performed a proteomics analysis of secreted factors from fibroblasts from young (<45 years) and aged (>55) human donors and found striking changes specifically in a group of proteins associated with the integrity of the skin extracellular matrix (ECM).

Human skin is characterized by an epidermal layer composed primarily of keratinocytes and a dermal layer comprised mostly of dense collagen-rich ECM largely secreted by dermal fibroblasts (4). Age-related changes in the physical properties of skin include decreases in collagen density (5, 6), ECM fiber area and thickness (7–9), as well as changes in the mechanical properties of the ECM, such as stiffness (6). Collagen cross-linking with fibulin, fibrillin, and elastin (10, 11) further enhances its structural stabilization (10, 12, 13). Changes in the turnover of these proteins are known to occur during natural aging (14). Specifically, collagen fibers in young skin are known to intersect in what is known as a "basket weave" pattern, where fibers cross each other at ~90° angles (15). This pattern breaks down during aging, giving way to a decreasingly dense matrix that has larger gaps between collagen fibers. These changes further contribute to mechanical and structural alterations, often visible as wrinkles in the skin.

Changes in matrix stiffness and density have long been associated with invasion of tumor cells. We recently developed a mathematical fiber network model that simulates the deformation of collagen networks (16) induced by cellular forces such as those experienced during the invasion of

cancer cells, which led us to reevaluate and refine the current thinking that linear increases in the stiffness of the ECM promote metastasis. Instead, we hypothesized that stiffness may be relative, depending on in which organ a tumor arises. For example, a breast cancer cell may arise in a "soft" environment that requires immense plasticity during lactation and menstruation, and this may need to stiffen for optimal invasion. A melanoma, however, arises in the skin, which by definition must form a strong, stiff barrier against external insults. Our data supported this, suggesting that when stiffness increases from a very soft "loose" ECM to a stiffer one, invasion increases, as elegantly reported in breast cancer studies (17). However, as fiber cross-linking and ECM stiffness increase further, a biphasic (i.e., as opposed to linear) tendency is evident in which cells under these conditions are no longer able to pass through tightly cross-linked pores. Our published model takes into account discrete morphologic alterations in the ECM, such as the realignment of the fibers and strain-stiffening, predicting a deformation zone around a contractile cell (18). This model was supported by our *in vitro* experiments showing that the fibrous nature and mechanical properties of the cross-linked ECM play key roles in the ability of the cells to invade (19). Hence our data, based on spheroid models, are more consistent with recent data showing that 3-D cell invasion is enhanced by increasing matrix stiffness and alignment until pore size becomes constrained and restricts cellular motility (20). We confirmed our models in 3-D spheroid assays and further showed that this effect was both proliferation and matrix metalloproteinase (MMP) independent (18). In the present study, we query the effect of aging on changes in the architecture of the ECM, and how those affect the migration of tumor and immune cells.

Our analysis of young versus aged fibroblast secretomes demonstrated that aging results in marked decreases in proteins involved in ECM production and remodeling, including fibulin, agrin, and the hyaluronan and proteoglycan link protein 1 (HAPLN1). We focused this study on HAPLN1, because it was the most differentially expressed protein in our study and was highly expressed by young fibroblasts. HAPLN1 is a cross-linking protein that stabilizes proteglycan monomer aggregates with hyaluronic acid (HA; ref. 21). HA alterations have been shown to increase the ability of fibroblasts to contract collagen matrices, suggesting that changes in HAPLN1 could affect collagen cross-linking and ECM contractility. In the present study, we specifically assess the role of HAPLN1, its loss during aging, and its effects on tumor cell motility. Further, we queried the effect of HAPLN1 loss on immune cell infiltrates, because immune cells have been shown to rely on dense collagen networks to move in and out of sites such as wounds, and the tumor microenvironment (22). Overall, using a mixture of matrix deposition assays, novel 3-D immune infiltration assays, and orthotopic mouse models, we show that increasing HAPLN1 in the aged microenvironment inhibits invasion and metastasis of tumor cells, while also promoting an active immune microenvironment. An understanding of ECM architecture in mediating age-related melanoma progression reveals a unique pathway to increase the effectiveness of current therapies and improve disease outcome in elderly patients.

RESULTS

Aging Affects the Structural Organization of the Dermal ECM

We performed a proteomics study on the secretome of aged versus young fibroblasts. Fibroblasts were obtained from young (<45 years) and aged (>55 years) healthy donors who participated in the Baltimore Longitudinal Study of Aging (23) and have been used previously to model the aging microenvironment (3, 24). To achieve robust and unbiased identification of factors that are differentially regulated in the secretome during normal aging, a SILAC quantitative proteomics experiment was performed on the secretomes of young/aged fibroblasts that had been cultured in "heavy" or "light" media with serum for nine cell doublings prior to incubation in the same media without serum for 8 hours. These serum-free media were used for proteome analysis, and 937 proteins were quantified with a protein and peptide false discovery rate (FDR) of <1%. A total of 90 proteins showed significant changes and were used to identify the top pathways that change during fibroblast aging (Fig. 1A; Supplementary Fig. S1A). For quality-control purposes, fibroblasts were assessed for viability in serum-free medium using calcein AM staining (Supplementary Fig. S1B), to ensure cells were still viable in the serum-free conditions used in the last phase of the SILAC experiment (Supplementary Fig. S1C–S1E). A list including all proteins exhibiting significant differences in abundance is shown in Supplementary Table S1. Notably, the most significantly changed proteins, between young and aged fibroblastic secretomes, were those involved in ECM remodeling (HAPLN1, agrin, laminin β2, fibulin, and tenascin).

To test the effects of the biomechanical changes of the aged skin on melanoma metastasis, we used our *in vitro* models to emulate the structural changes observed in the skin during aging. We prepared artificial reconstructions of skin (3-D skin reconstructs) using young and aged dermal fibroblasts to recreate the dermis, along with epidermal keratinocytes and melanoma cells as previously described (3). We first confirmed reported increases in the invasive ability of melanoma cells in the aged microenvironment (3). Moreover, the collagen in reconstructs made with aged fibroblasts had a lacier and looser appearance by hematoxylin and eosin (H&E) staining, which corresponded to less dense collagen autofluorescent signal by two-photon microscopy (Fig. 1B). Similar age-related changes in collagen could also be captured by two-photon microscopy in the normal mouse skin (in the absence of tumor), where aged mice demonstrated a loss of dermal collagen density with an increase in the dead space between more narrow collagen fibers (Fig. 1C). To determine whether the observed changes in collagen fibrils during aging translated to altered matrix contractility, we embedded young or aged fibroblasts in collagen gels and measured the ability of the fibroblasts to contract the gels. The percentage of contraction was greater in aged fibroblasts (Supplementary Fig. S2A and S2B).

Our data suggested that aged fibroblasts organize their ECM in a manner different from that of young fibroblasts. To better analyze changes in the ECM during aging, we employed an established *in vitro* cell-derived matrix (CDM) technique used to recreate ECM production by fibroblasts alone, in the

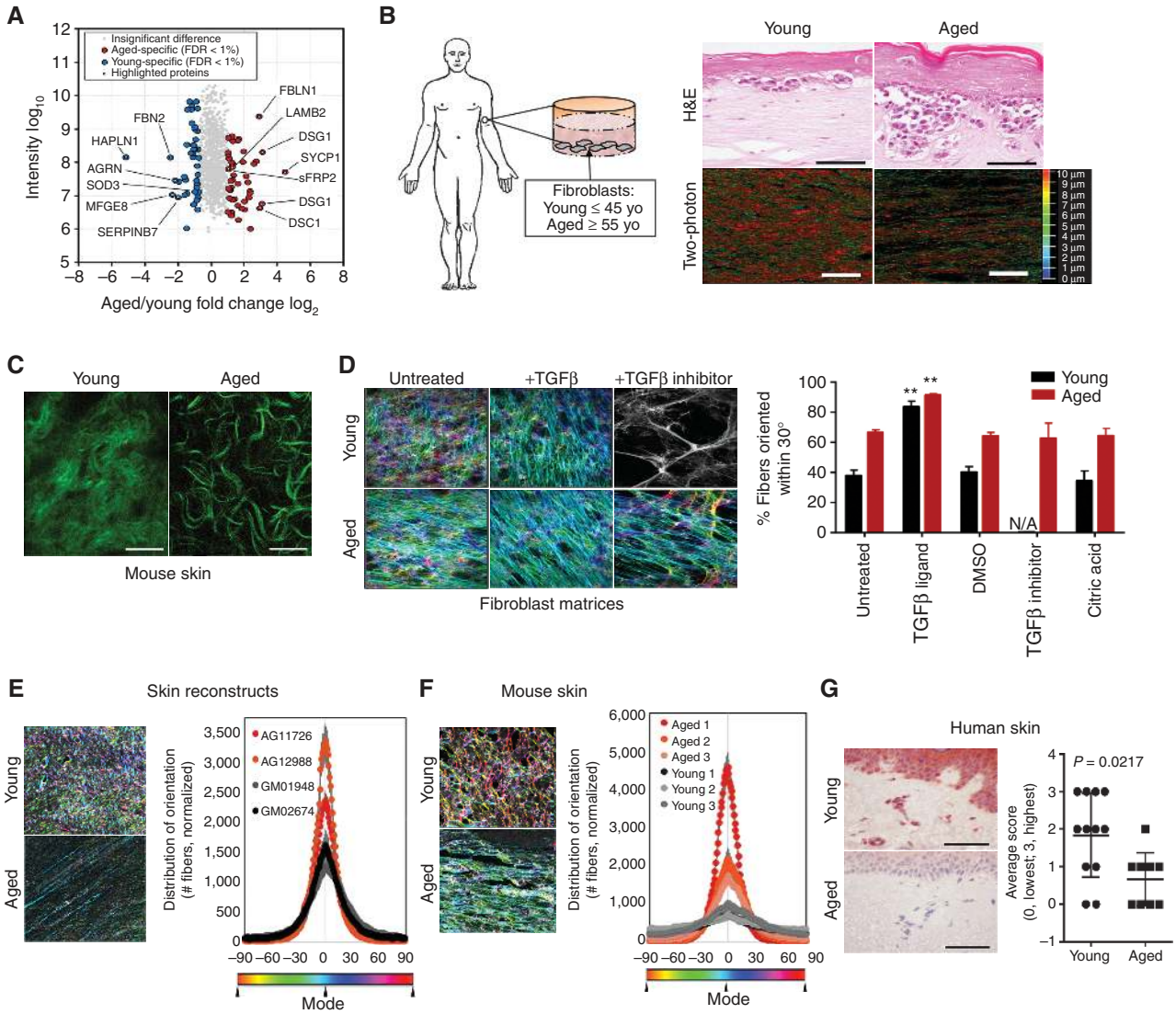

Figure 1. The ECM is significantly altered during aging. **A,** Secretome analysis from conditioned media from young and aged fibroblasts showing top overexpressed proteins in both young and aged microenvironments. **B,** Dermal fibroblasts from healthy human donors were used to prepare skin reconstructs. Invasion and collagen deposition was assessed by H&E staining (top; scale bars, 100 μm) as well as two-photon microscopy (bottom; scale bars, 25 μm). The color scale is indicative of the thickness of the collagen. **C,** C57BL/6 mouse skin was assessed for collagen composition using two-photon microscopy (scale bars, 25 μm). **D,** Young and aged dermal fibroblasts were allowed to form matrices and color-coded for fiber alignment. More colors represent less alignment. Panel shown in black and white indicates no significant matrix. Results are also quantified along with controls. N/A indicates no significant matrix formed. **E,** Skin reconstructs were prepared using multiple young (GM01948 and GM02674) and aged (AG11726 and AG12988) fibroblasts, and matrix alignment was measured. **F,** Young and aged C57BL/6 mice were injected with Yumm1.7 tumors and analyzed for matrix orientation at the skin/tumor interface. **G,** Normal human nonmelanoma skin from young and aged donors was stained for expression of HAPLN1 and scored based on intensity (3, highest; 0, lowest/absent). **, $P < 0.01$.

absence of tumor cells (25, 26). In this model, fibroblasts are treated with ascorbic acid to stabilize collagen secretion and ensure its incorporation into CDM fibrils. The manner by which the matrix is deposited (e.g., aligned/anisotropic vs. unaligned/isotropic) is reflective of the activation state of fibroblasts (27). Activated fibroblasts are determined by their ability to align CDMs to a greater extent (anistropic); >55% of fibers distributed 15 degrees from the mode angle. The aged matrices were characterized as producing anisotropic CDMs (Fig. 1D) and relatively decreased ECM thickness (Supplementary Fig. S2C). Young matrices, on the other hand, were isotropic and appeared to be denser than aged CDMs (Fig. 1D). Fibronectin levels did not change during aging (Supplementary Fig. S2D). TGFβ, which is known to promote ECM remodeling, is often used to activate dermal fibroblasts, driving them toward a cancer-associated fibroblast (CAF) phenotype (28). We find that young fibroblasts are responsive to TGFβ, becoming activated, and modify their CDMs to become anisotropic (Fig. 1D). The matrices laid down by aged fibroblasts are already aligned, and TGFβ serves to further increase their anisotropy (Fig. 1D). Interestingly, treatment of young fibroblasts with a TGFβ inhibitor disrupts their matrix

production, whereas aged fibroblasts are less responsive to the TGFβ inhibitor (Fig. 1D).

Because these observations were made using only fibroblasts, we wanted to explore whether they remained consistent in a 3-D setting that includes dermal and epidermal components. First, we explored the matrix alignment of the ECM in our skin reconstructs built using young or aged fibroblasts, and found that the CDM anisotropy seen using aged fibroblasts alone was recapitulated in the skin reconstructs (Fig. 1E). To extend these data to an *in vivo* model, we assessed the ECM in the skin of young and aged C57BL/6 mice. Aged mice (>52 weeks of age) showed an increased matrix alignment as compared with the skin of young mice that were 6 weeks of age (Fig. 1F). Overall, these data suggest that aged fibroblasts can significantly change the architecture of the ECM, in a manner consistent with that seen in activated, tumor-permissive fibroblasts. Conversely, young fibroblasts lay down a dense and isotropic matrix that is more consistent with the reported "basket weave" pattern (15).

Of all proteins measured (Fig. 1A; Supplementary Table S1), the most significantly changed was HAPLN1. We observed a 35-fold decrease in HAPLN1 in aged fibroblasts compared with young. We confirmed that HAPLN1 was increased in young fibroblasts compared with aged by performing ELISA on the conditioned media of 9 young and 9 aged fibroblast lines (Supplementary Fig. S3A). This was also true for normal young (<45 years) versus aged (>55 years) human skin (Fig. 1G). To determine whether TGFβ was able to directly affect HAPLN1 levels in young and aged fibroblasts, we treated fibroblasts directly with TGFβ1 and 2 and found no significant difference in the levels of HAPLN1 (Supplementary Fig. S3B and S3C). Next, we queried the correlation of HAPLN1 gene expression with age using The Cancer Genome Atlas databases of cutaneous melanoma and found that HAPLN1 was decreased during aging in melanoma patient samples (Supplementary Fig. S3D). Because HAPLN1 was decreased in the melanoma samples, we then asked whether HAPLN1 secretion from dermal fibroblasts affects the HAPLN1 levels in melanoma cells. We found that, indeed, melanoma cells exposed to young fibroblast conditioned media increase HAPLN1 production (Supplementary Fig. S3E and S3F). Overall, our results suggest that HAPLN1 is an abundant dermal protein secreted by fibroblasts, which is decreased during aging.

HAPLN1 Regulates the Structural Organization of the Dermal Microenvironment

A dense network composed mostly of collagen and elastin fibers along with large "space-filling" proteoglycans maintains the firmness of young skin. These discrete proteoglycans are bound to collagen with hyaluronic acid. HAPLN1 is purported to play a role in the cross-linking of hyaluronic acid and proteoglycans (21). Given the significant decrease of HAPLN1 in aged fibroblasts, we asked whether low levels of HAPLN1 contributed to the alteration of the young collagen basket weave structure rendering the observed increased alignment of dermal ECM fibers associated with aging. Using the ECM alignment assays described above, we tested CDM phenotypes *in vitro* using aged fibroblasts (in the absence of tumor cells) treated with increasing doses of HAPLN1 to achieve the physiologic range that was detected via ELISA in the young fibroblasts as measured in Supplementary Fig. S3A. Aged fibroblasts showed increases in collagen basket weave structure with increasing concentrations of HAPLN1 (Fig. 2A; a second fibroblast line is shown in Supplementary Fig. S4A). We analyzed the percentage of fibers oriented within the 30° range and observed recombinant HAPLN1 (rHAPLN1) dose–dependent decrease in the anisotropic levels of aged CDM fibers, suggesting that HAPLN1 decreases matrix activation (Fig. 2A; Supplementary Fig. S4B). Denatured HAPLN1 did not affect CDM fibers (Fig. 2B). Conversely, we knocked down HAPLN1 in young fibroblasts (Supplementary Fig. S4C) and questioned how this affects CDM architecture. As expected, the high degree of CDM isotropy seen in the young fibroblasts was lost with HAPLN1 knockdown (Fig. 2C). This could be rescued by simply adding back HAPLN1 (Fig. 2D; Supplementary Fig. S4D and S4E), emphasizing the importance of HAPLN1 in mediating fibroblastic CDM organization. The corresponding CDMs also showed HAPLN1-mediated changes in the thickness of the matrix, where increased HAPLN1 promoted thicker matrix deposition (Supplementary Fig. S4F), and knockdown of HAPLN1 resulted in decreased matrix deposition (Supplementary Fig. S4G) and changes in smooth muscle actin indicative of fibroblast activation (Supplementary Fig. S4H).

Because CDM assays are conducted largely by staining for fibronectin, we also wanted to stain and look for other changes in the ECM. First, we stained the CDMs for collagen by immunofluorescence, and noted a discernible change in the distribution of collagen that occurs during aging (Fig. 2E, top). This can be mimicked in young fibroblasts by knocking down HAPLN1, or the collagen loss reversed in aged fibroblasts by adding in recombinant HAPLN1 (Fig. 2E, bottom). Differential interference contrast (DIC) imaging of the CDMs also shows age-related changes in collagen that can be reversed by HAPLN1 (Fig. 2F). We also measured changes in the expression of alpha smooth muscle actin (α-SMA), known to be upregulated during desmoplasia, and in naïve fibroblastic cells in response to CAF CDMs (7, 27, 29). Consistent with these reports, we observed activated levels of α-SMA in aged fibroblasts, which decreased in a dose-dependent manner with rHAPLN1 treatment (Supplementary Fig. S4H). Conversely, knockdown of HAPLN1 in young fibroblasts, assessed during ECM production, showed an upregulation in α-SMA levels (Supplementary Fig. S4H).

To extend these results to *in vivo* models, we injected rHAPLN1 (100 ng) in aged (>52 weeks) C57BL/6 mice and observed a loss of collagen fiber anisotropy (Fig. 2G; Supplementary Fig. S4I and S4J). To determine whether this correlated to the ability of the fibroblasts to contract collagen, a feature of activated fibroblasts and of CAFs, we treated aged fibroblasts with increasing doses of rHAPLN1 and measured their ability to contract collagen. With increased HAPLN1, collagen contractility decreased, consistent with the results observed in young fibroblasts (Fig. 2H). Similarly, knocking down HAPLN1 in young fibroblasts increased their ability to contract collagen gels (Fig. 2H). Overall, these data suggest that HAPLN1 plays a major role in maintaining the dense basket weave structure of the collagenous ECM in young skin, while maintaining relatively low α-SMA levels, and that

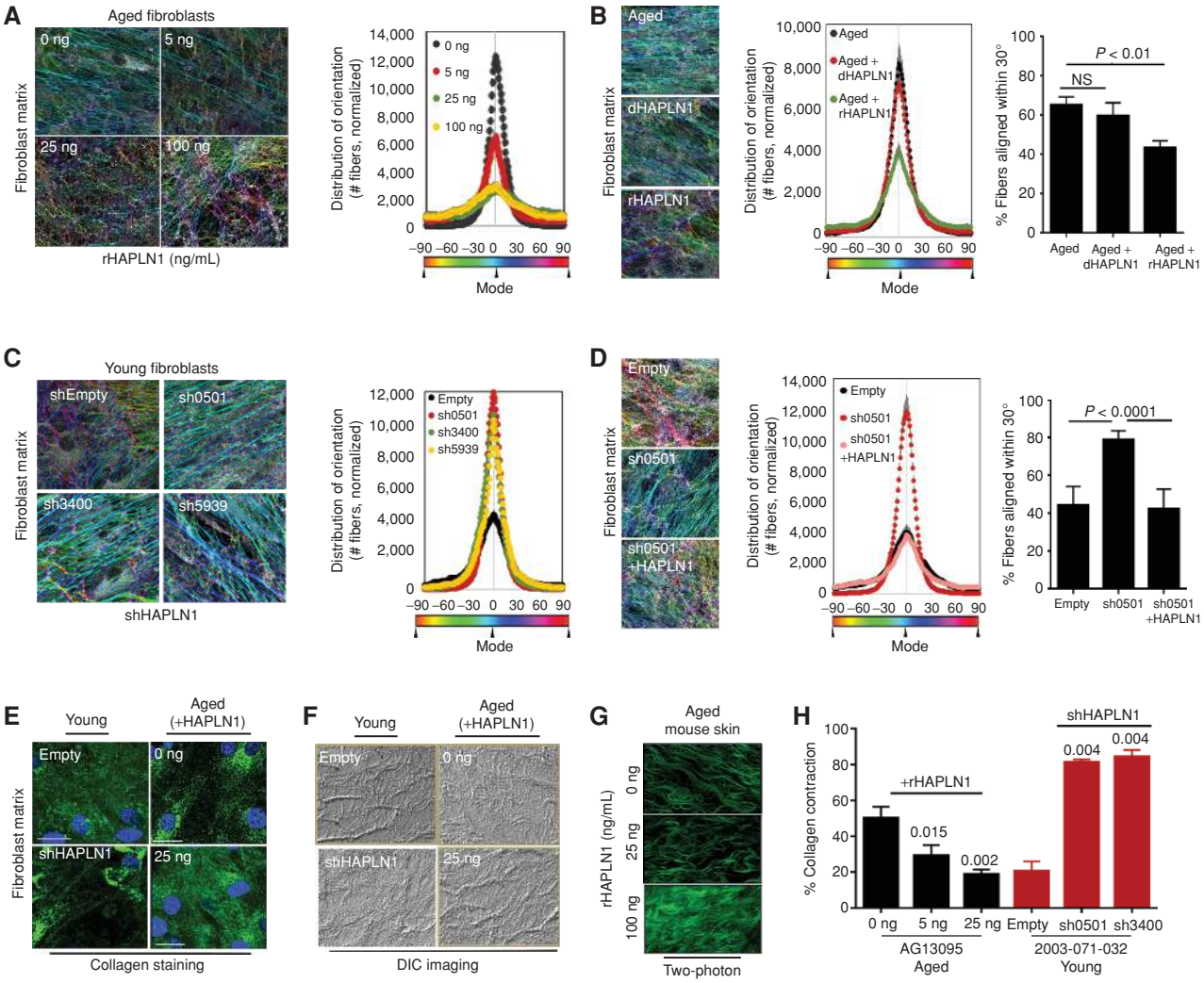

Figure 2. HAPLN1 loss in the aging microenvironment promotes ECM remodeling. **A,** Matrix production by aged fibroblasts was carried out in the presence of various concentrations of recombinant HAPLN1, and alignment of the matrix was measured. **B,** Aged fibroblasts were treated with active or denatured HAPLN1 (dHAPLN1; 25 ng/mL), allowed to form matrices, and matrix alignment was measured. **C,** Young fibroblasts with HAPLN1 knockdown were allowed to produce matrix and assessed for matrix production. **D,** Young fibroblasts with HAPLN1 knockdown were allowed to form matrices with or without the presence of rHAPLN1 (25 ng/mL) and assessed for matrix alignment. **E,** Matrices were produced by young fibroblasts with HAPLN1 knockdown and aged fibroblasts with rHAPLN1 treatment (25 ng/mL). Matrices were assessed for collagen I by immunofluorescence (scale bars, 25 μm). **F,** Skin reconstructs were prepared with young fibroblasts with HAPLN1 knockdown and aged fibroblasts with rHAPLN1 treatment (25 ng/mL). Skin reconstructs were embedded in paraffin and imaged for collagen bundles using DIC microscopy. **G,** Aged C57BL/6 mice were treated intradermally with 100 ng (50 ng/mL) rHAPLN1 for 7 days, followed by two-photon imaging for dermal collagen. **H,** Collagen was embedded with aged fibroblasts treated with varying concentrations of rHAPLN1 and young fibroblasts with HAPLN1 knockdown and layered in 48-well plates and assessed for contractility over 3 days [ANOVA (young + shHAPLN1), 0.0022; (aged + rHAPLN1), 0.0031]. For all experiments, ANOVA *post hoc* tests were performed using Bonferroni correction, and the significance values are shown in the figures.

its loss in aged skin can promote increased α-SMA and matrix alignment.

Mathematical Modeling Suggests That HAPLN1 Alters Matrix Organization and Inhibits Motility

The increase in matrix alignment and the loss of a tight basket weave structure suggested that the loss of HAPLN1 might promote cell invasion, given that an increase in porosity of the matrix might lead to a more invasion-permissive matrix. To predict how HAPLN1 affects invasion of cancer cells, we used a mathematical model that takes into account the effect of interfiber cross-links on the deformation of collagenous ECMs and the two-way feedback between cellular contractility and the strain-stiffening behavior of fibrous ECMs. We modeled the ECM as a network of cross-linked filaments that can deform by both bending and stretching. The network model reproduced the experimentally observed mechanical behavior of collagen networks in stretch. An initial linear stress–strain behavior was observed at small strains (smaller than ~5%) followed by strain-stiffening of large strains (greater than ~5%; Fig. 3A). The network model showed that the presence of HAPLN1 constrains the deformation of the network, leading to an increase in their stiffness (Fig. 3A). Furthermore, the additional cross-links constrained

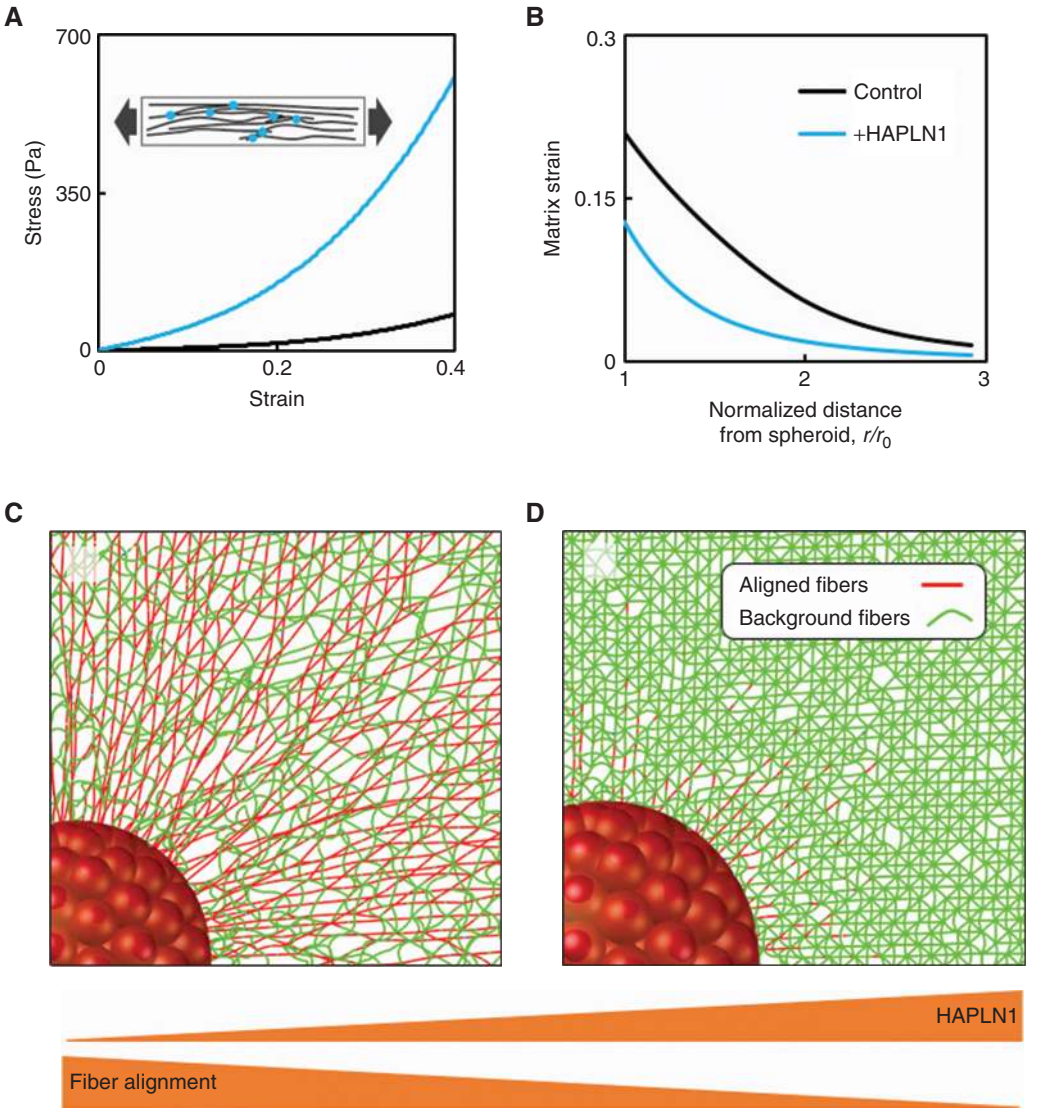

Figure 3. Chemomechanical model for HAPLN1 restriction of tumor invasion into the ECM. **A,** Stress–strain curves of fibrous networks with and without HAPLN1 obtained using stretch tests. The addition of HAPLN1 is modeled by the formation of cross-links between nearby fibers. The inset shows a schematic of the fibrous networks in the stretch tests. The fibers and cross-links are shown in black and red, respectively. **B,** The results from **A** are then used to inform our chemomechanical model about the mechanical behavior of fibrous matrices with and without HAPLN1. Strain in the matrix is plotted as a function of distance from the tumor spheroid. **C,** Fibers are aligned by the contractility of a tumor spheroid in the control case. The aligned and background fibers are displayed in red and green, respectively. Fibers are colored based on the stretching force present in the fibers. **D,** Reduced matrix deformation and fiber alignment are observed in the case where more fibers are cross-linked by HAPLN1. At the same level of strain, fewer fibers buckle in the matrix with HAPLN1 because cross-links constrain the lateral bending of individual fibers, preventing the alignment of fibers due to cell contractility.

the lateral bending and buckling of fibers and hindered the reorganization and reorientation of the stretched fibers. Therefore, less fiber alignment was observed as the networks were stretched in the presence of HAPLN1.

By incorporating the results of our network simulations, we next determined the influence of HAPLN1 on the structural organization of the ECMs in the presence of tumor spheroids. We modeled a spherical cluster of cells (with radius ~200 μm) embedded in ECMs containing or lacking HAPLN1. Following our previous work (18, 30), cells within the spheroid were modeled using a combination of a passive elastic element placed in parallel with an active contractile element. The passive element accounts for the stiffness of the cytoskeleton in response to external forces, whereas the active element represents the contractility of the cells (e.g., as suggested by the observed changes in α-SMA levels). The details of the mathematical model for the dependence of the contractility of the cells on the external stresses are presented in the Methods section.

Our model demonstrates that the addition of HAPLN1 substantially hinders the realignment of fibers by the tumor spheroid. As the tumor cells exert contractile forces on the surrounding ECM, they realign collagen fibers in the direction perpendicular to the boundary of the spheroid (31). Our model showed that the tumor spheroid induces more strain in the matrix that lacks HAPLN1 (Fig. 3B). The presence

of large strains in the absence of HAPLN1 leads to the substantial alignment of fibers that radiate from the tumor spheroid (Fig. 3C). In contrast, in the presence of HAPLN1, the higher stiffness of the matrix hinders contraction of the cells and imposes high stresses on the cells. In this case, our model shows that the spheroid induces less strain and fiber alignment in the matrix because the cross-linking of fibers due to HAPLN1 constrains the lateral bending and buckling of fibers; individual fibers buckle more easily if they are free to bend in the lateral direction. Taken together, our model suggests that in the presence of HAPLN1, cellular forces cannot reorganize the matrix, and the fibers remain randomly oriented, cross-linked, and unaligned/isotropic (Fig. 3D).

Structural ECM Organization Influences Melanoma Cell Invasion

Cell motility is thought to be a function of stiffness of the matrix as well as intrinsic invasiveness of the cells (32–34). We hypothesized that the aging microenvironment influences the intrinsic invasiveness by providing external cues to the cells to either limit or increase their motility. First, we assessed the ability of the ECMs to affect nondirectional motility of melanoma cells by obtaining cell-free CDMs from young and aged fibroblasts and introducing melanoma cells into these matrices. We observed changes in cell shape, where cells seeded on aged, desmoplastic matrices were increasingly elongated and motile, as assessed by time-lapse acquisition analysis (Supplementary Fig. S5A). Next, to study the implications of HAPLN1 changes in CDMs, we recreated the matrix microenvironment to study the effect of HAPLN1 on the motility of melanoma cells. We found that melanoma cells plated on CDMs deposited by aged fibroblasts decrease their velocity if the fibroblasts were treated with rHAPLN1 during ECM production (Supplementary Fig. S5B; Supplementary Movies S1–S4). Conversely, melanoma cells plated into young HAPLN1 knockdown fibroblast CDMs increased their velocity of movement (Supplementary Fig. S5C; Supplementary Movies S5–S7). Using 3-D skin reconstructs, we also showed that increasing HAPLN1 added together with aged fibroblasts altered the provided collagen, resulting in a decrease in melanoma invasion (Fig. 4A), whereas loss of HAPLN1 in young fibroblasts led to alterations that resulted in increased melanoma cell invasion (Fig. 4B). Results were supported by decreased invasion in melanoma spheroids embedded in collagen gels, embedded with aged fibroblasts, that were polymerized in the presence of increasing concentrations of HAPLN1 (Supplementary Fig. S5D), as well as by the increased invasion of melanoma spheroids that were cocultured with HAPLN1 knockdown fibroblasts (Supplementary Fig. S5E). HAPLN1 also affects the motility of melanoma cells in the absence of fibroblasts (Supplementary Fig. S5F).

Finally, our data have shown that tumors in aged mice metastasize more effectively to the lung (3). Given the effects of HAPLN1 on *in vitro* invasion, we asked whether HAPLN1 treatment of aged mouse skin could inhibit melanoma invasion. We implanted invasive Yumm1.7 melanoma cells into aged (>52 week) C57BL/6 mice and treated the mice with 50 ng/mL rHAPLN1 intradermally. Tumors in mice treated with rHAPLN1 were much smaller (Fig. 4C) and had decreased lung metastatic burden rates (Fig. 4D and E) compared with vehicle-treated controls. These data confirmed the predictions made by the mathematical models and suggested that loss of HAPLN1 facilitates invasion of melanoma cells in aged skin.

Immune Cell Infiltration Is Also Dependent on Cross-Linking of the Tumor-Associated ECM

The observed effects of HAPLN1 on tumor size were intriguing, and we asked whether HAPLN1 affected tumor cell proliferation. *In vitro* assays confirmed that HAPLN1 alone did not affect apoptosis of melanoma cells (Supplementary Fig. S6A and S6B), nor cellular proliferation in skin reconstructs (Supplementary Fig. S6C), nor did tumors in HAPLN1-treated mice show any loss of Ki67 activity (Supplementary Fig. S6D and S6E). These data suggested that perhaps decreased growth in the tumors in the HAPLN1-treated mice was reflective of an immunogenic response, such as increased T-cell infiltration. Although the pore size of the basket weave is a restrictive factor for tumor cells that have a relatively large nucleus, we predicted that it would be less so for immune cells, which have much smaller nuclei, as suggested by the existing literature (35). Further, T cells have been known to travel along interstitial collagen fibers in an MMP-independent manner to target the tumor (36–38). Hence, we hypothesized that T-cell infiltration might be affected by the HAPLN1 levels in the tumor microenvironment. To test this *in vitro*, we embedded melanoma spheroids in collagen along with T cells that have been clonally expanded and demonstrated to target the melanoma cell line *in vitro* (39). Melanoma spheroids in the presence of aged fibroblast media were embedded into collagen plugs containing autologous T cells and varying concentrations of rHAPLN1. As HAPLN1 concentrations increased, the T cells showed a dose-dependent increase in the velocity of the T-cell infiltrates targeting the melanoma cells that sprouted from tumor spheroids (Fig. 5A). Interestingly, T cells were not able to penetrate into the spheroids in the presence of aged conditioned media; however, adding rHAPLN1 induced an increase in T cell spheroid infiltration (Fig. 5B). Next, we embedded melanoma spheroids and T cells into collagen plugs containing young fibroblasts in which HAPLN1 had been knocked down. Loss of HAPLN1 in the young microenvironment decreased the velocity of T cells (Fig. 5C) and inhibited the infiltration of the T cells into the melanoma spheroid as compared with the empty-vector controls (Fig. 5D). Loss of HAPLN1 decreased collagen density and affected the accumulation of the T cells along collagen fibrils (Supplementary Fig. S7A). This phenotype was rescued by the addition of recombinant HAPLN1, such that the T cells reacquired velocity and penetrated the spheroid once again (Fig. 5E).

We next confirmed these data using a modified skin reconstruct model that we call a "sandwich reconstruct," into which we embedded the assorted fibroblasts together with melanoma cells in collagen and added autologous T cells to question their ability to target the red prelabeled melanoma cells (Supplementary Fig. S7B). Using a time-lapse imaging of the sandwich reconstruct, we observed striking increases

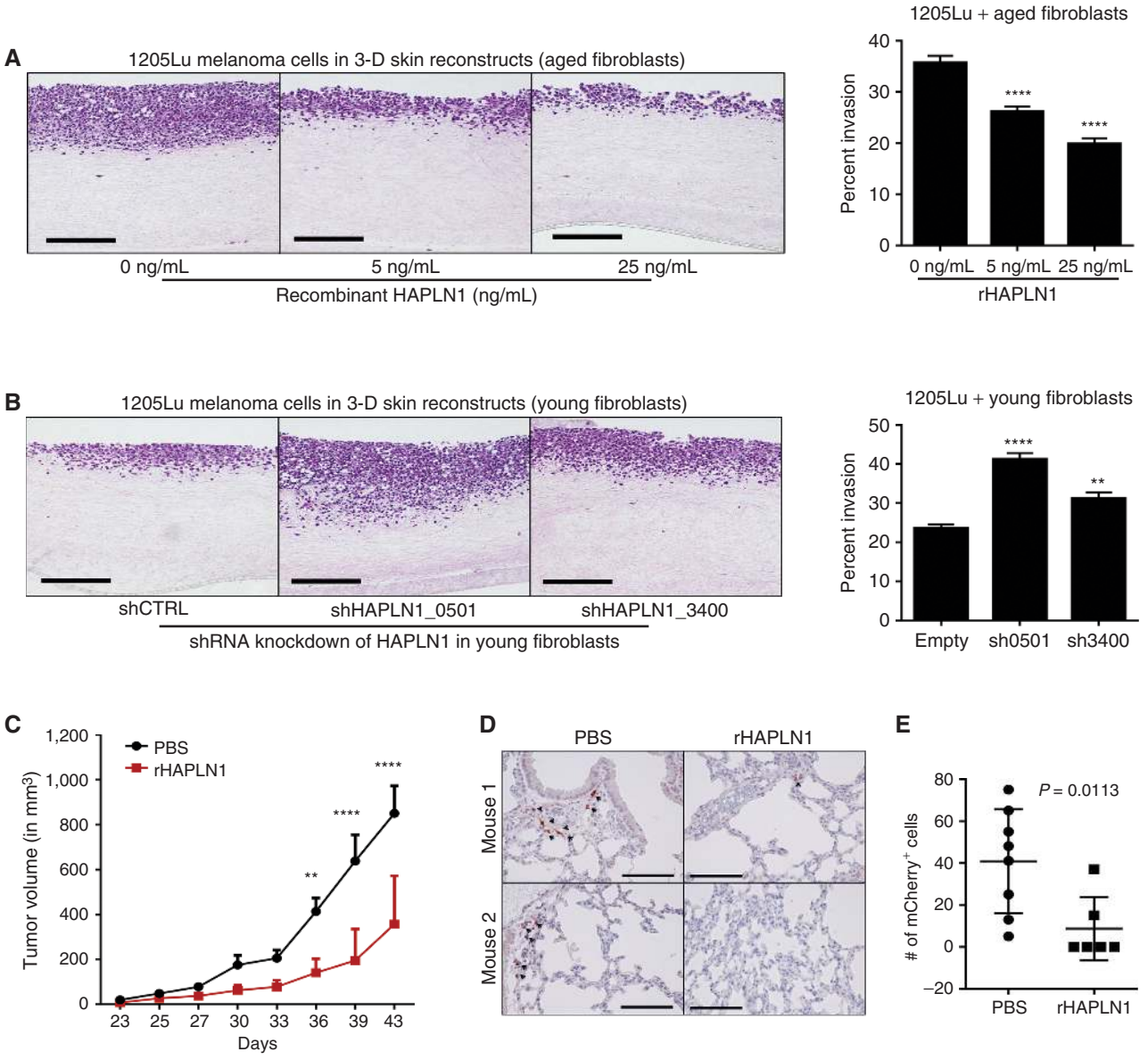

Figure 4. HAPLN1 decreases invasion and metastasis of melanoma cells. **A,** Skin reconstructs were prepared with aged fibroblasts treated with varying concentrations of rHAPLN1, and invasion was calculated as a percentage of reconstruct thickness (ANOVA, $P < 0.0001$; scale bars, 100 μm). **B,** Skin reconstructs prepared with young fibroblasts with HAPLN1 knockdown and 1205Lu melanoma cells. Invasion of melanoma cells into the collagen layer was calculated as a percentage of reconstruct thickness (ANOVA, $P < 0.0001$; scale bars, 100 μm). **C,** Aged C57BL/6 mice (>300 days old) were injected with Yumm1.7 melanoma cells overexpressing mCherry and treated with rHAPLN1 intradermally. Tumor growth was followed for 6 weeks (ANOVA, $P < 0.0001$). **D,** Lungs from mice injected with mCherry overexpressing Yumm1.7 cells were assessed for metastatic burden by IHC (scale bars, 100 μm). **E,** Total metastatic burden in mice from **D**. **, $P < 0.01$; ****, $P < 0.0001$.

in the motility of T cells within 6 to 8 hours in a HAPLN1-dependent manner (Fig. 5F; Supplementary Movies S8 and S9). As with the spheroid assays, knockdown of HAPLN1 in young fibroblasts inhibited T-cell movement toward the melanoma cells (Fig. 5G; Supplementary Movies S10 and S11). Importantly, HAPLN1 treatment of a sandwich reconstruct containing melanoma cells, aged fibroblasts, and autologous T cells showed a decrease in the number of melanoma cells, suggestive of the loss of these cells due to the cytolytic activity of T cells (Supplementary Fig. S7C, arrows). Taken together, these data suggest that HAPLN1 may play an important role in ECM-guided T-cell infiltration into tumor sites.

ECM Breakdown during Aging Differentially Affects T-cell Subpopulations

To determine whether we could increase infiltration of T cells into aged tumors by manipulating HAPLN1, we implanted Yumm1.7 cells in aged mice and treated the tumors with rHAPLN1 (50 ng/mL, twice weekly; control mice were injected with an equal volume of PBS as a control). Next, we proceeded to analyze these tumors for immune cell infiltration. Overall,

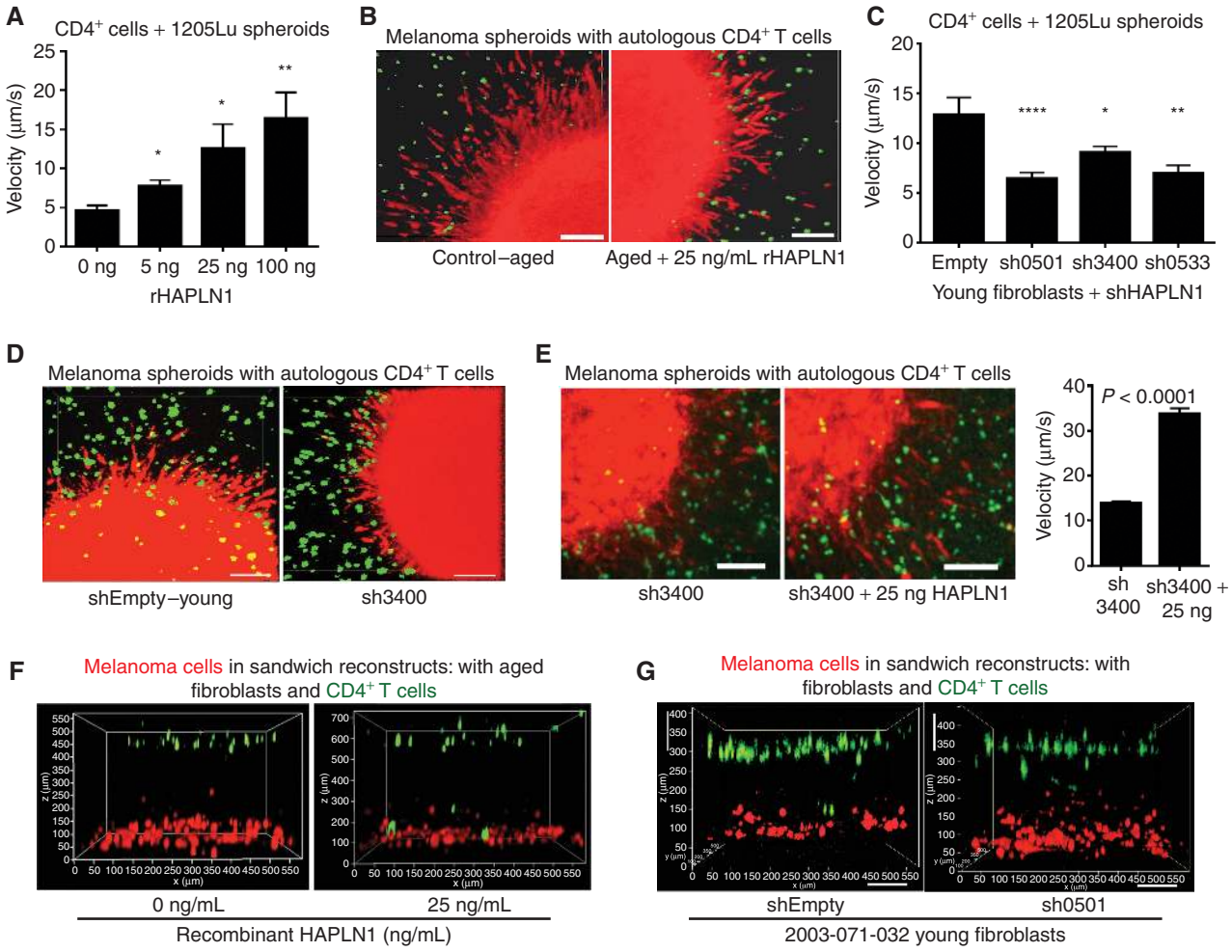

Figure 5. T-cell motility is affected by HAPLN1 in the ECM. **A,** Melanoma cells expressing mCherry were allowed to form spheroids, mixed with T cells stained with calcein AM and embedded in a collagen plug. The collagen plug was treated with varying concentrations of rHAPLN1. Time-lapse microscopy was used to image the movement of the T cells, and their velocity was quantified (ANOVA, $P < 0.0001$). **B,** Snapshots of the melanoma spheroids interacting with T cells in the presence of 25 ng/mL rHAPLN1 (scale bars, 25 μm). **C,** Melanoma cells expressing mCherry were allowed to form spheroids and embedded in collagen plug mixed with T cells stained with calcein AM and young fibroblasts with HAPLN1 knockdown. Time-lapse microscopy was used to quantify the velocity of the T cells (ANOVA, $P < 0.0001$). **D,** Snapshots of the melanoma spheroids interacting with T cells with HAPLN1 knockdown (scale bars, 25 μm). **E,** Melanoma cells expressing mCherry were allowed to form spheroids and embedded in collagen plugs prepared with young fibroblasts with HAPLN1 knockdown and reconstituted with rHAPLN1 (25 ng/mL). Time-lapse microscopy was used to assess velocity of T cells. Snapshots of the interaction between T cells and melanoma spheroids are also shown (scale bars, 25 μm). **F,** Melanoma cells expressing mCherry were layered at the bottom of the well followed by an additional layer of calcein AM–labeled T cells (green), and aged fibroblasts were treated with rHAPLN1 in a 3-D reconstruct model. **G,** Melanoma cells expressing mCherry were mixed in a collagen matrix and layered with a mix of young fibroblasts with HAPLN1 knockdown and calcein AM–labeled T cells (green) in a separate layer of collagen. Imaging was performed within 24 hours of preparing the reconstruct (scale bars, 100 μm). *, $P < 0.05$; **, $P < 0.01$; ****, $P < 0.0001$.

likely due to the decrease in tumor size upon treatment with rHAPLN1, there was a decrease in overall (CD45$^+$) immune cell infiltration (Supplementary Fig. S8A). However, when we analyzed the percentage of CD45$^+$ cells that also expressed CD3$^+$, we observed a clear increase in this T lymphocyte cell population in HAPLN1-treated mice (Fig. 6A), and of these CD4$^+$ and CD8$^+$ cells were increased by HAPLN1 treatment (Supplementary Fig. S8B). We repeated the experiment, this time measuring immune cells as a percentage of all live cells. We observed that in response to rHAPLN1 treatment, CD8$^+$ T cells increased significantly (Fig. 6B) as measured by flow cytometry. The change in CD4$^+$ cells, although significant when taken as part of the CD45$^+$ population (Supplementary Fig. S8B), was less so when calculated as a percentage of live cells, but still trended toward an increase (Supplementary Fig. S8C). We next measured dendritic cells, macrophages, and monocytic myeloid-derived suppressor cells (M-MDSC), none of which changed (Fig. 6C–E). However, we found that HAPLN1 treatment significantly decreased the infiltration of polymorphonuclear myeloid-derived suppressor cells (PMN-MDSC) and regulatory T cells (Treg) into the tumor (Fig. 6F and G), although PMN-MDSC populations were not changed in young versus aged mice (Supplementary Fig. S8D). This resulted in a significant increase in the ratio of CD8$^+$:Tregs (Fig. 6H). Finally, to determine if this increase in the CD8$^+$:Treg ratio correlated to increased cytolytic activity in the tumor, we stained the HAPLN1 versus

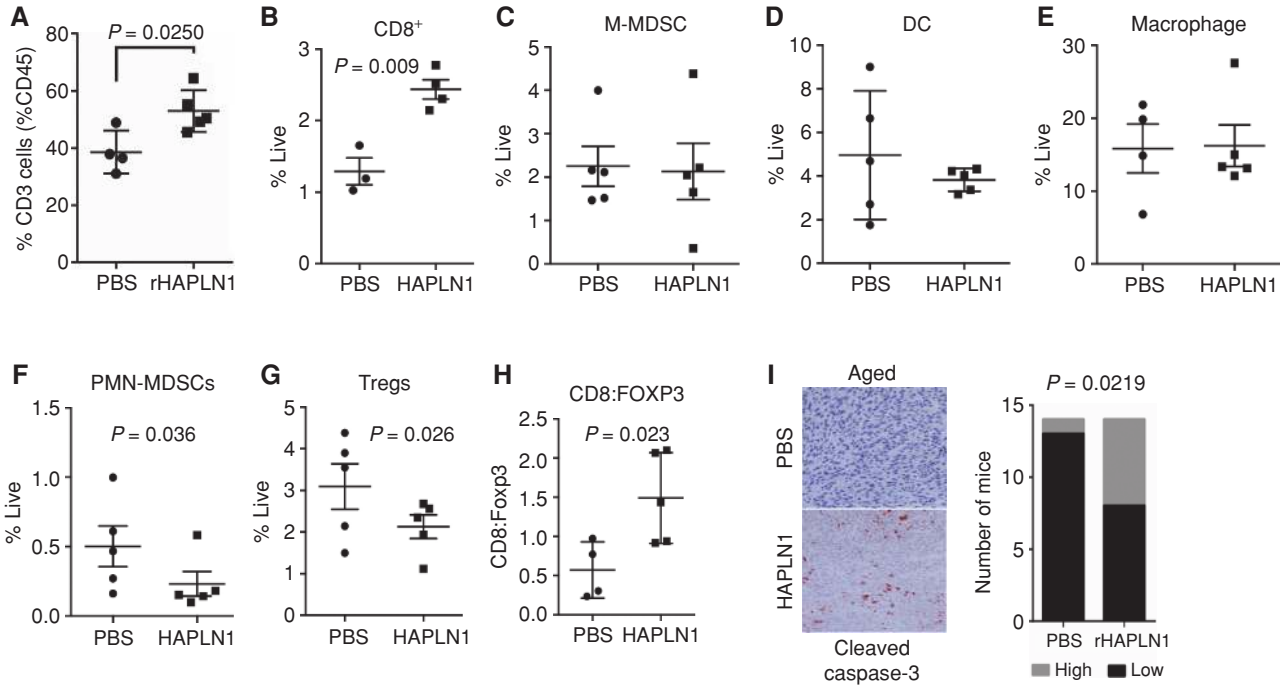

Figure 6. HAPLN1 affects immune cell infiltration *in vivo*. **A,** Aged C57BL/6 mice were injected with Yumm1.7 allografts and treated intradermally with rHAPLN1. Tumors in mice were analyzed for $CD3^+$ cells. **B,** Aged mice with Yumm1.7 allografts were treated with rHAPLN1 and assessed for infiltration of $CD8^+$ cells by flow cytometry. Yumm1.7 allografts were also assessed for infiltration of (**C**) M-MDSCs ($CD11b^+Ly6G^{neg}Ly6C^{hi}$), (**D**) dendritic cells ($CD11c^+F4/80^-/^{lo}$), and (**E**) macrophages ($CD11b^+F4/80^+$). **F,** Aged mice injected with Yumm1.7 allografts were treated intradermally with rHAPLN1 and assessed for PMN-MDSC cell (CD11b+, $Ly6G^{hi}$, $Ly6C^{lo}$) infiltration. **G,** Aged mice with Yumm1.7 allografts were treated with rHAPLN1 and assessed for infiltration of Tregs ($CD4^+$, $FOXP3^+$) by flow cytometry. **H,** Tumors from mice were compared for expression of CD8:FOXP3 per tumor. **I,** Tumors were also assessed for activity of cleaved caspase-3 using IHC. Cleaved caspase-3 staining was quantified by counting positive cells across 20 sampled areas and dichotomized to low (0–1+ staining) and high (2–3+ staining) in mice ($n = 15$) with or without rHAPLN1 treatment.

control tumors for cleaved caspase-3. HAPLN1-treated tumors had higher levels of cleaved caspase-3 than controls (Fig. 6I), suggesting that tumor cells were being lysed. Again, HAPLN1 does not affect tumor cell apoptosis in the absence of a microenvironment (Supplementary Fig. S6A and S6B), so these data suggest that the tumor microenvironment is required for the deleterious effects of HAPLN1. Overall, our data suggest that tumor cell invasion is inhibited by increased HAPLN1, and the immune tumor microenvironment is enhanced. Manipulating these mechanical changes could promote immune cell infiltration while inhibiting tumor cell extravasation to increase the effectiveness of current therapies.

DISCUSSION

We have presented here an analysis of ECM changes in the physical makeup of the aging skin and the subsequent effects on tumor-cell invasion and immune-cell infiltration. It is well accepted that changes in matrix stiffness, such as loss of pliability, affect the metastatic properties of tumor cells (17). This occurs not only by providing optimal contractile forces for the migration of tumor cells, but also by affecting signaling, which can alter growth and even responses to drugs (40). Further, ECM alignment associated with assorted cancers effectively predicts patient outcomes and metastasis (41–43). We show here that age-related changes in the ECM facilitate the migration of tumor cells but may also hamper immune cell infiltration. We identify a novel role for HAPLN1, showing that it can suppress invasion of melanoma cells in young skin, and that it is lost during aging, creating an invasion-permissive microenvironment. We hypothesize that this is due to the fact that the nuclei of tumor cells can no longer pass through the small pores created by a highly cross-linked matrix. Although our studies have focused solely on HAPLN1, given its large change in aged fibroblasts, we have a deep appreciation of the breadth of studies that can ensue from this work. Other factors secreted by our young fibroblasts are also known to be involved in cross-linking the ECM, such as aggrecan and LOXL2. Intriguingly, increases in tumor cell–associated LOXL2 have been associated with increased invasion (44). However, it may be that LOXL2 loss in the stromal cells, as suggested by our proteomic signature during aging, is perhaps more reflective of the loss of integrity in dermal collagen.

Our studies suggest that aged fibroblasts bear great similarity to CAFs in terms of myofibroblastic activation (e.g., upregulation of α-SMA), the alignment of CDMs, and the ability to increase tumor cell metastasis. Interestingly, targeting CAFs either with chimeric antigen receptor T cells designed to eliminate them, or with drugs such as perfidine, has been shown to decrease the spread of metastatic breast cancer (45). Targeting aged fibroblasts might have similarly beneficial effects for patients with melanoma. However, rather than eradicating them, reversing their phenotype

to one where they produce "youthful" ECMs may be the most useful strategy, as our data indicate that the matrix the fibroblasts produce is likely required for antitumor immune infiltration. T cells first use the vasculature to infiltrate the tumor (38, 46) and proceed to migrate along the ECM fibers of the tumor microenvironment (46), particularly the collagen fibers (36, 37). Our results show a decreased infiltration of $CD4^+$ and $CD8^+$ T cells on an age-impaired matrix, which could be improved by changing the matrix dynamics with HAPLN1. The maximum motility of a cell is a function of matrix porosity and cell deformation that can be achieved by that cell type, with the cell deformation being dependent on the nuclear size, rigidity, and shape (35). The shape of the T cells, along with their polarity, is eventually important in predicting the response of the T cells toward antigen presentation. Other factors also need to be considered—for example, the chemokine receptor and adhesion molecule makeup of $CD4^+$ and $CD8^+$ T cells differ, and may affect their ability to migrate into the tumor microenvironment. Normal $CD4^+$ T cells have been shown to have a great propensity to infiltrate collagen, and this was initially thought to be due to their ability to express MMPs (47). However, the concept of MMPs as an important factor in T-cell migration has been challenged, as the movement of T cells through collagen has been shown to be MMP-independent (35). This is in keeping with our own data on the effects of increasingly stiff matrices on tumor cell migration, as we have shown that to be partially MMP-independent as well (18). More recently, the ability of $CD4^+$ and $CD8^+$ cells to differentially express chemokine receptors, integrins, and selectins during homing to different organ sites has been explored. Both $CD4^+$ and $CD8^+$ T cells express P- and E-selectin when homing to the skin (48), but in a gene-expression analysis study of activated immune cells, $CD4^+$ cells were shown to also express CCR5 and CX3CR1, whereas $CD8^+$ cells do not (49). On the other hand, the IL7R was more highly expressed in $CD8^+$ cells. Although the results from these studies, due to the nature of the immune response elicited, cannot be directly correlated to our work, they do highlight the fact that $CD4^+$ and $CD8^+$ cells differentially express receptors that are known to depend on the ECM for their transduction. Therefore, it is not unreasonable to expect that the age-related changes in the ECM may differentially affect the chemokine, integrin, and adhesion molecule profiles in the different populations of immune cells in the tumor microenvironment. We surmise that the differences in tumor volumes in mice with HAPLN1 treatment were based on both restriction of tumor spreading by efficiently cross-linked matrix and improved immune cell kinetics; however, additional studies are needed on these factors. What is intriguing is that increasing HAPLN1 appears to selectively inhibit the movement of PMN-MDSCs, which have a larger nuclear volume, and this may contribute to the inhibition of Tregs in the HAPLN1-treated tumors.

Our studies imply that changes in the immune microenvironment of aged tumors cannot be purely ascribed to age-related immunosenescence. It is known that during aging, there is a decrease in the ability of T cells to traffic from lymph nodes and other sites to sites of injury, infection, or cancer. Studies assessing age-related decline in immune cell trafficking tend to focus on response to chemokines, or immunosenescence of the T cells, but the role of the ECM as a modulator of T-cell motility is beginning to emerge. For example, the role of advanced glycation end products found in aging may affect T-cell activity (50) and T-cell expression of proteins that can interact with ECM has been identified (51). However, the effects of age-related ECM changes on either tissue-resident lymphocytes found in the skin or trafficking of lymphocytes to tumor sites have not been explored (52). Our results highlight the importance of physical changes in the ECM as a mediator of immune and tumor cell trafficking that transcend signaling or other T cell–intrinsic changes such as immunosenescence, because simply reconstituting HAPLN1 in the ECM affects immune cell infiltration. Studies of aging and immunosenescence are largely performed on peripheral blood samples, just as studies of intratumoral T-cell populations have largely been conducted in young mice. The first excludes the role of the ECM on T cells, and the latter excludes the effects of age on T-cell infiltration, which we attempt to address in this study. Further, with the identification of tissue-resident memory T cells (Trm; ref. 53), which reside in tissues such as the skin, lung, and gut during the lifetime of an organism, understanding the role of the ECM in regulating Trm becomes increasingly important. It will be interesting to explore the maintenance versus egress of these cells during aging in organ sites such as the skin.

We have previously examined the effects of immunotherapy in young versus aged microenvironments (54). Surprisingly, in patients under the age of 50, there is a much lower ratio of $CD8^+$:Tregs, rendering these patients less responsive to anti–PD-1 than older patients. Depleting Tregs in young mice increases sensitivity to anti–PD-1 therapy. We were therefore somewhat surprised that HAPLN1 did not also lower the CD8:Treg ratio, but this is likely due to the fact that HAPLN1 may alter the ability of PMN-MDSCs to get to the tumor site. This is further supported by the fact that in tumors in young versus aged mice, we see no difference in the infiltration of PMN-MDSCs, M-MDSCs, or macrophages (Supplementary Fig. S8D), although we do see a shift in CD4s, CD8s, and Tregs as we have previously published (54). Additionally, there are likely numerous secreted and other changes that occur during aging which cannot be completely reversed simply by HAPLN1 addition, but this reemphasizes the critical role that mechanical changes play. Because immunotherapy has had such remarkable success in melanoma, enhancing the immune microenvironment by promoting a favorable $CD8^+$:Treg ratio may increase response to immune-checkpoint inhibitors. These analyses help to provide an outlook whereby understanding the mechanical structure of the tumor microenvironment, particularly during aging, can provide means by which to increase effectiveness of current therapies.

METHODS

Cell Culture

1205Lu and WM3918 cells were maintained in DMEM (Invitrogen), supplemented with 5% FBS and 4 mmol/L L-glutamine. WM35 cells were maintained in MCDB153 (University of Pennsylvania Cell Center Services)/L-15 (Cellgro; 4:1 ratio) supplemented with 2% FBS and 1.6 mmol/L $CaCl_2$ (tumor growth media). YUMM1.7 cells were maintained in DMEM supplemented with 10% FBS and 4 mmol/L

L-glutamine. Fibroblasts were maintained in DMEM, supplemented with 10% FBS and 4 mmol/L L-glutamine. Keratinocytes were maintained in keratinocyte SFM supplemented with human recombinant epidermal growth factor 1–53 (EGF 1–53) and bovine pituitary extract (Invitrogen).

Cell lines were cultured at 37°C in 5% CO_2, and the medium was replaced as required. Cell stocks were fingerprinted using AmpFLSTR Identifiler PCR Amplification Kit from Life Technologies TM at The Wistar Institute Genomics Facility. Although it is desirable to compare the profile to the tissue or patient of origin, our cell lines were established over the course of 40 years, long before acquisition of normal control DNA was routinely performed. However, each short tandem repeat (STR) profile is compared with our internal database of over 200 melanoma cell lines as well as control lines, such as HeLa and 293T. STR profiles are available upon request. Cell culture supernatants were *Mycoplasma* tested using Lonza MycoAlert assay at the University of Pennsylvania Cell Center Services.

Proteomics

Fibroblasts were incubated for nine doublings in SILAC-labeled media (MS 10030, Life Technologies). The young fibroblasts were labeled with heavy [$^{13}C_6$,$^{15}N_4$]-L-arginine and $^{13}C_6$-L-lysine, whereas the aged fibroblasts were labeled with light arginine and lysine. Cells were then seeded at 2.2×10^6/150 cm^2 dish, incubated overnight, washed with Hank's Balanced Salt Solution (HBSS), and incubated for 8 hours in appropriate SILAC media. Conditioned media were then centrifuged at 10,000 × *g* for 30 minutes, filtered through a 0.2-μm filter, and concentrated using an Amicon Ultra 10K filter (Millipore) to a protein concentration of approximately 1 μg/μL. Samples were then combined, and proteins were separated on an SDS-PAGE gel for 3.5 cm. The gel lane was sliced into 35 fractions, digested with trypsin, and analyzed by LC/MS-MS on an LTQ-Orbitrap XL mass spectrometer (Thermo Fisher Scientific) as described previously (55).

Data analysis was performed using MaxQuant version 1.3.0.5 (56). MS-MS data were searched against the human UniRef 100 protein database (July 2012, Protein Information Resource, Georgetown University) using full trypsin specificity with up to two missed cleavages, 6 ppm precursor mass tolerance, 0.5 Da fragment ion mass tolerance, static carboxamidomethylation of Cys, and variable oxidation of Met and protein N-terminal acetylation. Consensus protein lists were generated with false discovery rates of 1% at both peptide and protein levels. Proteins were also required to be identified by at least two razor plus unique peptides, and a minimum ratio count of three. Protein fold changes were calculated from the normalized H/L ratio. A 3 standard deviation (SD) cutoff was determined from a control heavy/light labeled young fibroblast sample and was used to identify proteins with significant change in expression.

Organotypic 3-D Skin Reconstructs

Organotypic 3-D skin reconstructs were generated as previously described (57). Briefly, an acellular layer of collagen was prepared in transwells for 6-well dishes (BD #355467 and Falcon #353092) and allowed to solidify for 1 hour at room temperature. Next, 6.4×10^4 fibroblasts were mixed with collagen and plated on the acellular layer and incubated for 45 minutes at 37°C in a 5% CO_2 tissue culture incubator. DMEM containing 10% FBS was added to each well of the tissue culture tray and incubated for 4 days. Next, reconstructs were preincubated for 1 hour at 37°C in HBSS containing 1% dialyzed FBS to wash off DMEM with 10% FBS and replaced with reconstruct media I. Keratinocytes (4.17×10^5) and melanoma cells (8.3×10^4) were mixed in 1:5 ratio and added to the inside of each insert. Media were changed to reconstruct media III and replaced every other day until day 18 when the reconstructs were harvested. For conditions requiring treatment with recombinant protein, fibroblasts were pretreated with rHAPLN1 for 72 hours, and rHAPLN1 (varied doses) was freshly added to the media during media replacement. After the reconstructs were harvested, they were fixed in 10% formalin, paraffin embedded, sectioned, and stained. Quantification of the invasion was performed using ImageJ software (available at http://imagej.nih.gov/ij/; developed by Wayne Rasband, NIH, Bethesda, MD).

3-D Spheroid Assays

Tissue culture–treated 96-well plates were coated with 50 μL 1.5% Difco Agar Noble (Becton Dickinson). Melanoma cells were seeded at 5×10^3 cells/well and allowed to form spheroids over 72 to 96 hours. Spheroids were harvested and embedded using collagen type I (GIBCO, #A1048301). The collagen plug was prepared as 300 μL mix per layer, and two layers were added into each well [1× Eagle Minimum Essential Medium (EMEM; 12-684, Lonza); 10% FCS; 1× L-glutamine; 1.0 mg/mL collagen I; $NaHCO_3$ (17-613E, Lonza), diluted in PBS as required]. The first layer was added to each well and allowed to solidify. After 5 to 10 minutes, spheroids were mixed with the remaining 300 μL mix and added to the well to solidify. Once the plug was solidified, media were added to the well and incubated at 37°C at 5% CO_2 and imaged daily until invasion had surpassed the field of view. For treatment with recombinant protein, rHAPLN1 (#2608-HP, R&D Systems) was added to both the top and bottom layers while preparing the collagen plug. For experiments with shHAPLN1 fibroblasts, melanoma cells were prelabeled with mCherry before spheroid formation, while 6,000 fibroblasts labeled with GFP were mixed in each layer of the collagen plug. Spheroids were imaged in mCherry fluorescence channel to quantify invasive area. For spheroids embedded with T cells, melanoma cells prelabeled with mCherry were used. A $CD4^+$, HLA class I–restricted CTL clone was isolated from the peripheral blood of a patient with primary melanoma. This clone was then shown to be able to stably lyse autologously matched melanoma cells for up to 9 months in culture. T cells were obtained by selection of immunoreactive T cells against target melanoma cells (WM793/1205Lu) as previously described (39). T cells were labeled with calcein AM (1:10,000; L3224, Invitrogen) for 1 hour at 37°C, 5% CO_2. Cells were washed with 1× PBS before being added to the collagen plug mix. The collagen plug mix was used as described above. Spheroid images were acquired on Nikon TE2000 inverted microscope, and time-lapse imaging of spheroids was performed on Leica TCS SP8 X WLL laser scanning spectral confocal microscope. Quantitation of invasive surface area as well as tracking of T cells was performed using NIS Elements Advanced Research software.

Denaturation of rHAPLN1

Recombinant HAPLN1 was purchased from R&D Systems (#2608-HP) and reconstituted in sterile PBS at 100 μg/mL. For denaturation, reconstituted rHAPLN1 was mixed in 9M urea and boiled for 10 minutes at 95°C followed by sterilization through 0.22-μm filter. Denatured HAPLN1 was stored at room temperature until use. 9M urea was used as control at the same concentration as denatured HAPLN1.

Production of Fibroblastic CDMs

Fibroblast CDMs were prepared as previously described (25, 26). Briefly, 12 mm coverslips (No. 1) were added to 24-well plates and coated with 0.2% gelatin solution for 1 hour. Coverslips were washed with Dulbecco's Phosphate Buffered Saline (DPBS) and treated with 1% glutaraldehyde solution for 30 minutes at room temperature. After washing with DPBS, coverslips were incubated with 1M ethanolamine for 30 minutes at room temperature. After 5 washes with DPBS, 1.0×10^5 fibroblasts were plated onto the coverslips and incubated overnight at 37°C, 5% CO_2. The following day, media were replaced with fresh media containing 50 μg/mL L-ascorbic acid. L-ascorbic acid was added daily to the wells to a final concentration of 50 μg/mL with fresh media replacement every other day. After 5 treatments, CDMs and fibroblasts were

analyzed or fibroblasts were removed and the remaining matrices were used as described below.

Extraction of Fibroblast from CDMs and Reconstitution of Melanoma Cells

Fibroblast CDMs were prepared as stated above. After the matrix production was complete, fibroblasts were removed from the matrices to allow seeding of other cells for functional assays. Wells were washed with Ca^{2+} and Mg^{2+} free DPBS twice. This was followed by treatment with extraction buffer (0.05% TritonX-100, 20 mmol/L NH_4OH in DPBS lacking Ca^{2+} and Mg^{2+}) for 10 minutes, followed by 1:1 dilution with DPBS, and incubated overnight at 4°C. The next day, DPBS was used to wash the wells multiple times to remove cellular debris. The extracted matrices were stored at 4°C until used for no longer than 2 weeks. Three thousand melanoma cells (1205lu melanoma cells expressing mCherry) were seeded in a 24-well plate, and time-lapse imaging was performed on Nikon TE300 inverted microscope mounted in an incubation chamber. Quantification of melanoma cell velocity was performed using NIS Elements Advanced Research software and graphed in GraphPad/Prism6.

Immunofluorescence

Samples were fixed with 4% paraformaldehyde, containing 0.5% TritonX, for 5 minutes at room temperature followed by treatment with 4% paraformaldehyde at room temperature for 20 minutes. Samples were blocked using "IF blocking buffer" comprising PBS complemented with 0.2% Triton-X100, 0.2% BSA, 0.2% casein, 0.2% gelatin, and 0.02% sodium azide and filtered prior to use. Primary antibodies were incubated overnight at 4°C using the following concentrations: αSMA (1:100, A2547; Sigma), fibronectin (1:200, F3648; Sigma), collagen I (1:100, ab34710; abcam), diluted using "IF blocking buffer" as above. After washing with PBS, samples were incubated with the appropriate secondary antibodies (1:2,000; Invitrogen) for 1 hour at room temperature, followed by additional PBS wash, and mounted in Prolong Gold antifade reagent containing DAPI (Invitrogen). Images were captured on a Leica TCS SP5 II scanning laser confocal system.

Anisotropy Levels and Thickness Measurements of ECMs

ECMs were stained for fibronectin and imaged using Leica SP5 II Confocal System. Samples were imaged using 63× objective with 2× zoom power, and each image composing the resultant z-stacks was set to step 0.5 μmol/L. Images composing these z-stacks were analyzed and counted to calculate the overall matrix thickness, using a minimum of nine stacks for averaging the matrix thickness per condition. In addition, images were analyzed using ImageJ Plugin OrientationJ (available for download at http://bigwww.epfl.ch/demo/orientation/; ref. 58). Maximum stack 3-D reconstruction images of the ECM fibers were normalized for orientation measurements using R and graphed. Anisotropic measurements in images were normalized using Adobe Photoshop. Mode value for each image(x) obtained from OrientationJ was used to calculate $-2x$ values, and this value was incorporated in hue settings to normalize each image to mode value. Source code for R is provided in Supplementary Files.

IHC

Patient samples were collected under Institutional Review Board exemption approval for protocol #EX21205258-1. Skin reconstructs were paraffin embedded and sectioned. Paraffin-embedded sections were rehydrated through a xylene and alcohol series, rinsed in H_2O, and washed in PBS. Antigen retrieval was performed using target retrieval buffer (#H3300, Vector Labs) and steamed for 20 minutes. Samples were blocked in a peroxidase blocking buffer (#TA060H2O2Q, Thermo Scientific) for 15 minutes, followed by Protein block (#TA-060-UB, Thermo Scientific) for 5 minutes, and incubated in appropriate primary antibody diluted in antibody diluent (S0809, Dako) at 4°C overnight in a humidified chamber. Following washing in PBS, samples were incubated in biotinylated anti-rabbit (abcam) followed by streptavidin–HRP solution at room temperature for 20 minutes. Samples were then washed in PBS and incubated in 3-amino-9-ethyl-l-carbozole (AEC) chromogen for 15 minutes (#TA060SA, Thermo Scientific). Finally, samples were washed in H_2O, incubated in Mayer's hematoxylin (MHS1, Sigma) for 1 minute, rinsed in cold H_2O, and mounted in Aquamount (#143905, Thermo Scientific). Primary antibodies used were purchased as described: HAPLN1 (TA325115, Origene), Ki67 (CloneSP6, Thermo Scientific), mCherry (NBP2-25157, Novus Biologicals), CD4 (14-9766-82, Thermo Scientific), CD8a (14-0808-82, Thermo Scientific), and cleaved caspase-3 (9661S, Cell Signaling).

T-cell Migration in Organotypic Culture (Reconstruct)

T-cell cultures were prepared using a modified approach as previously described (39). Briefly, a $CD4^+$, HLA class I–restricted CTL clone was isolated from the peripheral blood of a patient with primary melanoma. This clone was then shown to be able to stably lyse autologously matched melanoma cells for up to 9 months in culture. Organotypic cultures were prepared in 4-well 35-mm glass bottom dishes for optimal imaging (Greiner cellview #50590467; Thermo Fisher Scientific). An acellular bottom layer was prepared with collagen matrix [1.6 mL 10× EMEM (12-684F, Lonza), 0.16 mL L-glutamine, 1.82 mL heat-inactivated FCS, 0.2 mL $NaHCO_3$ (17-613E, Lonza), 14.8 mL Rat Tail Collagen I (final concentration 2.0 mg/mL, #354249; Corning)] and 200 μL of this mix was plated in each well and allowed to solidify for 1 hour. 1205lu melanoma cells labeled with mCherry were harvested and plated on the acellular layer at 6×10^5 cells per well in the Tu2% media. On the following day, fibroblasts (6×10^4 cells) were harvested and mixed with T cells ($1–3 \times 10^6$ cells), mixed with 250 μL collagen matrix and layered on the melanoma cells. The layers were allowed to solidify, and imaging was started after 3 to 4 hours of addition of T cells at 37°C, 5% CO_2. After 5 days, reconstructs were harvested and embedded in OCT and sectioned for histologic evaluation. H&E-stained slides were imaged on EVOS XL Core Cell Imaging System. Time-lapse imaging was performed on Leica TCS SP8 X WLL laser scanning spectral confocal microscope for 24 hours.

Two-Photon Microscopy

Samples of skin (2.5 × 2.5 cm) were shaved and collected from C57BL/6 mice, held in buffer solution under nylon mesh, and imaged with a Leica TCS SP8 MP 2-photon intravital microscope (Leica Microsystems, Inc.). The specific region of interest was in the dermis. Alternatively, for skin reconstructs, 15-μm-thick sections were collected on glass slides, deparaffinized, and passed through a series of alcohol washes, followed by mounting in Aquamount (#143905, Thermo Scientific). Collagen was visualized using second harmonic generation (SHG) from 900 nm excitation in a Chameleon XR Ti:Saphire laser (Coherent, Inc.). SHG emission was captured in 12 bits, at 700 Hz, through a 25×/1.00 water-immersion objective in reflected mode using an HyD detector with a standard DAPI filter set. Mouse tissue images shown are composites of 15 z-stacks, and skin reconstruct images are composites from 21 stacks, with 10 mm step size. The images were further processed using Huygens Professional Deconvolution software (Scientific Volume Imaging, B.V.).

In Vivo *rHAPLN1* Assay

All animal experiments were approved by the Institutional Animal Care and Use Committee (IACUC #112503X_0) and were performed in an Association for the Assessment and Accreditation of Laboratory Animal Care–accredited facility. Yumm1.7 cells were injected

into young (6–8 weeks old) or aged (>300 days old) mice (Charles River). For experiments with rHAPLN1 treatments, aged mice (>300 days old) were purchased from Taconic. YUMM1.7 (1×10^5 cells) overexpressing mCherry were injected intradermally into mice that were treated with 100 ng (total) rHAPLN1 (#2608-HP, R&D Systems) or PBS as control at the time of allograft injection. Tumor sizes were measured every 3 to 4 days using digital calipers, and tumor volumes were calculated using the following formula: volume = 0.5 × (length × width^2). Time-to-event (survival) was determined by a 5-fold increase in baseline volume (~1,000 mm^3) and was limited by the development of skin necrosis. Mice were euthanized, lungs were harvested, and metastases were counted. Half of the tissue was embedded in paraffin and half in OCT compound and flash-frozen for sectioning. Lungs were sectioned and stained with mCherry antibody (NBP2-25157, Novus Biologicals) to determine melanoma metastasis. All reagents injected in live mice were tested for endotoxin levels at University of Pennsylvania Cell Center Services using The Associates of Cape Cod LAL test, and results are available upon request.

Flow Cytometry Analysis

Tumors were harvested from mice immediately after euthanasia and were processed through the tumor dissociation kit (#130-096-730, Miltenyi Biotec) using the manufacturer's protocol. Single cells were incubated with primary antibodies for 30 minutes at room temperature. Cells were washed once with PBS and analyzed using LSRII (18-color; Becton Dickinson). Primary antibodies were purchased from BioLegend [CD4-BV510 (100553); CD8b-PerCP/Cy5.5 (100733); CD45-APC (103112); CD3-AF700 (100216); Zombie-yellow (423103); CD11b-PE/CY7 (301321); CD11c-APC/CY7 (337217); F4/80-PE (123109); FOXP3-PacBlue (126409)] and BD Bioscience [Ly6G-PE (561104) Ly6C-FITC (561085)]. Results were analyzed on FlowJo and graphed in GraphPad/Prism6.

Collagen Contractility Assay

Three thousand fibroblasts were mixed with collagen matrix [1× EMEM (12-684, Lonza); 10% FCS; 1× L-glutamine; 1.0 mg/mL collagen I; $NaHCO_3$ (17-613E, Lonza), diluted in PBS as required], and 300 μL mixture was plated in a 48-well plate and allowed to set. Images were taken at time 0 and used as control, and the collagen plug was separated from the well using a fine needle. After 3 days, wells were imaged again, and contractility was measured based on the area of the collagen plug at day 3 normalized to area on day 0. Images were acquired on UVP Gel Doc-It Imager.

SILAC Proteomics Analysis

Fibroblasts were incubated for nine doublings in SILAC-labeled media (MS 10030, Life Technologies). The young fibroblasts were labeled with heavy [13C6,15N4]-L-arginine and 13C6-L-lysine, whereas the aged fibroblasts were labeled with light arginine and lysine. Cells were then seeded at 2.2×10^6/150 cm^2 dish, incubated overnight, washed with HBSS, and incubated for 8 hours in appropriate serum-free SILAC media (conditioned media). Conditioned media were then centrifuged at 10,000 × *g* for 30 minutes, filtered through a 0.2-μm filter, and concentrated using an Amicon Ultra 10K filter (Millipore) to a protein concentration of approximately 1 μg/μL. The heavy (young) and light (aged) labeled samples were then combined at a 1:1 ratio based on total protein followed by separation on an SDS-PAGE gel for 3.5 cm. A control consisting of a 1:1 mixture of heavy (young) and light (young) samples was processed in the same manner. The gel lanes were sliced into 35 fractions, digested with trypsin, and analyzed by LC/MS-MS on an LTQ-Orbitrap XL mass spectrometer (Thermo Fisher Scientific) as described previously (55).

Data analysis was performed using MaxQuant version 1.3.0.5 (56). MS-MS data were searched against the human UniRef 100 protein database (July 2012, Protein Information Resource, Georgetown University) using full trypsin specificity with up to two missed cleavages, 6 ppm precursor mass tolerance, 0.5 Da fragment ion mass tolerance, static carboxamidomethylation of Cys, and variable oxidation of Met and protein N-terminal acetylation. Consensus protein lists were generated with false discovery rates of 1% at both peptide and protein levels. Proteins were also required to be identified by at least two razor plus unique peptides, and quantitated by a minimum ratio count of three. Protein fold changes were calculated from the normalized H/L ratio. A 3 SD fold change cutoff was determined from the control heavy/light-labeled young fibroblast samples and was used to identify significantly changed proteins in the young/old fibroblast secretome.

ELISA

Nunc MaxiSorp ELISA plates (eBioscience) were coated with 50 μL of 3 μg/mL HAPLN1 (1:500, #P51999PU-N; Acris Antibodies) overnight at 4°C. Plates were washed in PBS containing 0.1% Tween20 and blocked in ELISA diluent (00-4202-56; eBioscience) for 2 hours. Conditioned media were harvested after 72 hours and used without any dilution at 50 μL per well and incubated overnight at 4°C. Next day, the plates were washed in PBS containing 0.1% Tween20 and incubated with detection antibody, for 1 hour at room temperature. Plates were washed and incubated with secondary antibody HAPLN1 (MAB2608, R&D Systems) diluted 1:1,000 for 1 hour. After washing, 100 μL of 1× TMB (00-4201-56; eBioscience) solution was added to the plates and incubated for 15 minutes. The reaction was stopped using 50 μL of 2N H_2SO_4, and absorbance was measured at 450 nm.

Lentiviral Production and Infection

HAPLN1 shRNA was obtained from The RNAi Consortium (TRC) shRNA library available through the Molecular Screening Facility at The Wistar Institute. Plasmids without open reading frame (ORF) expression were used as control plasmids. pLU-EF1α-mCherry was used for mCherry overexpression in multiple cell lines. PLX304-GFP overexpression plasmid was obtained as a gift from the laboratory of Dr. Meenhard Herlyn. Lentiviral production was carried out as described in the protocol developed by the TRC library (Broad Institute). Briefly, 293T cells were cotransfected with shRNA/ORF vector and lentiviral packaging plasmids (pCMV-dR8.74psPAX2, pMD2.G). The supernatant containing virus was harvested at 36 and 60 hours, combined and filtered through a 0.45-μm filter. For transduction, the cells were layered overnight with lentivirus containing 8 μg/mL polybrene. The cells were allowed to recover for 24 hours and then selected using puromycin selection marker.

Western Blotting

Melanoma samples were harvested in appropriate amounts of whole-cell lysis buffer (6% SDS, 30% glycerol, 0.18M Tris pH6.8, 5% DTT, bromophenol blue). Protein was quantified using a Qubit assay kit (#Q33212, Thermo Scientific), and 50 μg protein was boiled for 10 minutes at 95°C and loaded on 4%–20% Bis-Tris gels. Samples were run at 165V and transferred on PVDF membranes. Membranes were blocked for 1 hour in 5% milk and incubated with appropriate antibody overnight at 4°C. The next day, membranes were washed in TBS with 0.1% Tween and incubated with secondary antibody for 1 hour at room temperature. Membranes were washed and developed using chemiluminescence-based detection reagents (#PI80196, Thermo Scientific). Chemiluminescence was detected using ImageQuant LAS 4000 (GE Healthcare Life Sciences). Primary antibody to HSP90 was purchased from Cell Signaling Technology (1:4,000, 4877S), HAPLN1 (1:500, TA325115) from Origene, and anti-rabbit secondary antibody from Jackson ImmunoResearch (#211-032-171).

Quantitative PCR

Cells were plated as required for every experimental procedure. After the treatment was completed, cells were harvested using TRIzol (Invitrogen, #15596026) and subjected to phenol:chloroform

extraction. Approximately 500 μL TRIzol was used for a T25 flask, and a 5:1 phenol:chloroform ratio was used. After the addition of 100 μL chloroform, samples were centrifuged for separation of different layers for 15 minutes at 4°C, and RNA layer was collected and mixed with fresh 70% ethanol in a 1:1 ratio and subjected to cleanup using an RNeasy Mini kit (# 74106, Qiagen) as per the manufacturer's protocol. RNA (1 μg) was used to prepare cDNA using iscript DNA synthesis kit (#1708891, Bio-Rad). cDNA was diluted 1:5 before use for further reactions. Each 20 μL well reaction was composed of 10 μL Power SYBR Green Master mix (4367659, Invitrogen), 1 μL primer mix (final concentration 0.5 μmol/L), and 1 μL cDNA. Standard curves were generated for all primers, and each set of primers was normalized to 18 Primer pair (#AM1718, Ambion, Invitrogen). Primer sequences are described here: HAPLN1 (forward CAGAC CTCACTCTGGAAGATTATG; reverse: GGGAATACCAGACCTTGTA AGT), fibronectin (forward: TTGCTCCTGCACATGCTTTG; reverse: CATGAAGCACTCAATTGGGCA).

Chemomechanical Model for the Stress-Dependent Contractility of the Cells

Following our previous work (18, 30), the chemomechanical behavior of the cells was characterized by introducing a spatially varying strain ε_{ij} and a contractility tensor ρ_{ij}. In the coarse-grained system, the trace of the contractility tensor ($\rho_{11}+\rho_{22}+\rho_{33}$) represented the density of the recruited myosins in the actomyosin system. Here, we adopted an energy-based approach and obtained the total energy of the cells, accounting for mechanical deformations, motor binding energy, and mechanochemical feedback as follows:

$$U = \underbrace{\frac{1}{2}C_{ijkl}\varepsilon_{ij}\varepsilon_{kl} + \rho_{ij}\varepsilon_{ij}}_{\text{Mechanical energy}} + \underbrace{\overbrace{\frac{\beta}{2}\left[\frac{1}{3}(\rho_{kk}-3\rho_0)^2 - \frac{1}{3}(\rho_{kk}{}^2 + \rho_{ij}\rho_{ij})\right]}^{\text{Motor binding energy}} - \overbrace{\frac{1}{2}\left[\frac{1}{3}(\alpha_v-\alpha_d)\sigma_{kk}\rho_{kk} + \alpha_d\sigma_{ij}\rho_{ij}\right]}^{\text{Mechanochemical feedback}}}_{\text{Chemical energy}}$$

The mechanical energy accounts for the strain energy stored in the cytoskeleton (C_{ijkl} being the elastic constants) and the mechanical work done by the myosin motors as they generate the cellular contractions. ρ_0 is the density of the motors attached to the cytoskeleton in the quiescent state. The motor binding energy, proportional to the "chemical stiffness β," ensured that perturbations of the motor density from ρ_0 lead to an increase in the energy. And, finally, the mechanochemical feedback part accounts for the activity of the molecular pathways such as Rho-pathway and the increase in the cell contractility in response to external tensile stresses. The mechanochemical coupling parameter α_v is responsible for coupling of the overall density of the motors to the external stress whereas α_d determines the polarization in motor recruitment.

By minimizing this total free energy function with respect to the strains (ε_{ij}) and cell polarization (ρ_{ij}), we determined the strain and the contractility of the cells and finally the force exerted by the cell cluster on the surrounding ECM. The parameters used in the model are presented in Table 1.

Statistical Analysis

For *in vitro* studies, a Student *t* test or Wilcoxon rank-sum test (Mann–Whitney) was performed for two-group comparison. Estimate of variance was performed, and unequal variances for the *t* test were adjusted accordingly using Welch correction. ANOVA or Kruskal–Wallis test with *post hoc* Holm–Sidak adjusted *P* values was used for multiple comparisons. For *in vivo* studies, the indicated sample size for each experiment was designed to have 80% power at a two-sided α of 0.05 to detect a difference of large effect size about 1.51 between two groups on a continuous measurement. The change in tumor volume at each time point after treatment relative to baseline was calculated and then the change in the treatment group relative to the age-matched control group was compared using a mixed-effect model to evaluate the treatment effect between experimental groups. GraphPad/Prism6 and Stata14 were used for plotting graphs and statistical analysis. Significance was designated as follows: *, $P < 0.05$; **, $P < 0.01$; ***, $P < 0.001$.

Table 1. Parameters used in the chemomechanical model

Parameter	Symbol	Value	Reference
E	Cell elastic modulus	0.3 kPa	(18)
ν	Cell Poisson's ratio	0.3	(18)
ρ_o	Cell initial motor density	0.15 kPa	(18)
α_v	Chemomechanical feedback parameter	15 per kPa	(18)
α_d	Chemomechanical feedback parameter	25 per kPa	(18)
β	Motor turnover parameter	30 per kPa	(18)
r_0	Cluster initial radius	200 μm	(18)

Disclosure of Potential Conflicts of Interest

J.A. Wargo is an advisory board member for Bristol-Myers Squibb, Roche-Genentech, Novartis, AstraZenenca, Illumina, and Merck, and has received honoraria from the speakers bureau of Dava Oncology. M.T. Tetzlaff is a consultant/advisory board member for Myriad Genetics, Novartis LLC, and Seattle Genetics. A. Raj has received other remuneration from LGC/Biosearch Technologies. A.T. Weeraratna is a consultant/advisory board member for Phoremost Technologies and Melanoma Research Foundation. No potential conflicts of interest were disclosed by the other authors.

Authors' Contributions

Conception and design: A. Kaur, C.H. Kugel III, M.R. Webster, R. Somasundaram, V. Shenoy, E. Cukierman, A.T. Weeraratna
Development of methodology: A. Kaur, B.L. Ecker, J. Hayden, E. Ban, J. Franco-Barraza, X. Xu, V. Shenoy, E. Cukierman, A.T. Weeraratna
Acquisition of data (provided animals, acquired and managed patients, provided facilities, etc.): A. Kaur, B.L. Ecker, M.R. Webster, F.V. Almeida, R. Somasundaram, J. Hayden, E. Ban, N. Shah, F. Keeney, H.-Y. Tang, X. Xu, M. Fane, M. Herlyn, D.W. Speicher, J.A. Wargo, M.T. Tetzlaff, L.E. Haydu, A. Raj, E. Cukierman, A.T. Weeraratna
Analysis and interpretation of data (e.g., statistical analysis, biostatistics, computational analysis): A. Kaur, C.H. Kugel III, M.R. Webster, J. Hayden, E. Ban, H. Ahmadzadeh, J. Franco-Barraza, I.A. Mellis, F. Keeney, A. Kossenkov, H.-Y. Tang, X. Yin, Q. Liu, M. Fane, M. Herlyn, D.W. Speicher, M.T. Tetzlaff, E. Cukierman, A.T. Weeraratna
Writing, review, and/or revision of the manuscript: A. Kaur, B.L. Ecker, S.M. Douglass, F.V. Almeida, E. Ban, J. Franco-Barraza, A. Kossenkov, Q. Liu, X. Xu, M. Fane, D.W. Speicher, J.A. Wargo, M.T. Tetzlaff, L.E. Haydu, E. Cukierman, A.T. Weeraratna
Administrative, technical, or material support (i.e., reporting or organizing data, constructing databases): B.L. Ecker, P. Brafford, M. Herlyn, L.E. Haydu, A.T. Weeraratna
Study supervision: V. Shenoy, E. Cukierman, A.T. Weeraratna

Acknowledgments

We thank Dr. Katie Marchbank for technical assistance with the preparation of fibroblasts for proteomics and Dr. Chi Van Dang for critical reading of the manuscript. NIH funding (NCI): We thank the outstanding Core Facilities of the Wistar Institute supported by P30CA010815; A.T. Weeraratna, S.M. Douglass, and Q. Liu are supported by R01CA174746 and R01CA207935. A. Kaur is supported by F99CA212437. X. Xu, X. Yin, Q. Liu, M. Herlyn, D.W. Speicher, M. Fane, and A.T. Weeraratna are also supported by P01 CA114046 and P50CA174523. C.H. Kugel III is supported by T32CA009171. M.R. Webster is supported by K99CA208012. D.W. Speicher is supported by RO1CA131582. E. Cukierman is supported by R01 CA113451 and P30CA06927. Other funding: A.T. Weeraratna is also supported by the Melanoma Research Fund, Melanoma Research Alliance/L'Oréal Paris-USA Women in Science Team Science Award, the Ira Brind Endowment, and the Wistar Science Discovery Fund. M. Herlyn is supported by a gift from the Adelson Medical Research Foundation. E. Cukierman is supported by DODW81XH-15-1-0170 and a gift from Mrs. Concetta Greenberg in memory of Dr. Marvin Greenberg. V. Shenoy is supported by the NSF Center for Engineering Mechanobiology (CMMI-154857).

The costs of publication of this article were defrayed in part by the payment of page charges. This article must therefore be hereby marked *advertisement* in accordance with 18 U.S.C. Section 1734 solely to indicate this fact.

Received February 26, 2018; revised July 23, 2018; accepted September 19, 2018; published first October 2, 2018.

REFERENCES

1. Balch CM, Thompson JF, Gershenwald JE, Soong SJ, Ding S, McMasters KM, et al. Age as a predictor of sentinel node metastasis among patients with localized melanoma: an inverse correlation of melanoma mortality and incidence of sentinel node metastasis among young and old patients. Ann Surg Oncol 2014;21:1075–81.
2. Tsai S, Balch C, Lange J. Epidemiology and treatment of melanoma in elderly patients. Nat Rev Clin Oncol 2010;7:148–52.
3. Kaur A, Webster MR, Marchbank K, Behera R, Ndoye A, Kugel CH, et al. sFRP2 in the aged microenvironment drives melanoma metastasis and therapy resistance. Nature 2016;532:250–4.
4. Situm M, Buljan M, Cavka V, Bulat V, Krolo I, Mihic LL. Skin changes in the elderly people–how strong is the influence of the UV radiation on skin aging? Coll Antropol 2010;34(Suppl 2):9–13.
5. Diridollou S, Vabre V, Berson M, Vaillant L, Black D, Lagarde JM, et al. Skin ageing: changes of physical properties of human skin in vivo. Int J Cosmet Sci 2001;23:353–62.
6. Panwar P, Lamour G, Mackenzie NC, Yang H, Ko F, Li H, et al. Changes in structural-mechanical properties and degradability of collagen during aging-associated modifications. J Biol Chem 2015;290:23291–306.
7. Lee HO, Mullins SR, Franco-Barraza J, Valianou M, Cukierman E, Cheng JD. FAP-overexpressing fibroblasts produce an extracellular matrix that enhances invasive velocity and directionality of pancreatic cancer cells. BMC Cancer 2011;11:245.
8. Marcos-Garces V, Molina Aguilar P, Bea Serrano C, Garcia Bustos V, Benavent Segui J, Ferrandez Izquierdo A, et al. Age-related dermal collagen changes during development, maturation and ageing - a morphometric and comparative study. J Anat 2014;225:98–108.
9. Oh JH, Kim YK, Jung JY, Shin JE, Kim KH, Cho KH, et al. Intrinsic aging- and photoaging-dependent level changes of glycosaminoglycans and their correlation with water content in human skin. J Dermatol Sci 2011;62:192–201.
10. Roark EF, Keene DR, Haudenschild CC, Godyna S, Little CD, Argraves WS. The association of human fibulin-1 with elastic fibers: an immunohistological, ultrastructural, and RNA study. J Histochem Cytochem 1995;43:401–11.
11. Sephel GC, Davidson JM. Elastin production in human skin fibroblast cultures and its decline with age. J Invest Dermatol 1986;86:279–85.
12. Neame PJ, Barry FP. The link proteins. EXS 1994;70:53–72.
13. Yeowell HN, Marshall MK, Walker LC, Ha V, Pinnell SR. Regulation of lysyl oxidase mRNA in dermal fibroblasts from normal donors and patients with inherited connective tissue disorders. Arch Biochem Biophys 1994;308:299–305.
14. Martin H, Dean M. An N-terminal peptide from link protein is rapidly degraded by chondrocytes, monocytes and B cells. Eur J Biochem 1993;212:87–94.
15. Berthod F, Germain L, Li H, Xu W, Damour O, Auger FA. Collagen fibril network and elastic system remodeling in a reconstructed skin transplanted on nude mice. Matrix Biol 2001;20:463–73.
16. Wang H, Abhilash AS, Chen CS, Wells RG, Shenoy VB. Long-range force transmission in fibrous matrices enabled by tension-driven alignment of fibers. Biophys J 2014;107:2592–603.
17. Levental KR, Yu H, Kass L, Lakins JN, Egeblad M, Erler JT, et al. Matrix crosslinking forces tumor progression by enhancing integrin signaling. Cell 2009;139:891–906.
18. Ahmadzadeh H, Webster MR, Behera R, Jimenez Valencia AM, Wirtz D, Weeraratna AT, et al. Modeling the two-way feedback between contractility and matrix realignment reveals a nonlinear mode of cancer cell invasion. Proc Natl Acad Sci U S A 2017;114:E1617–26.
19. Cao X, Lin Y, Driscoll TP, Franco-Barraza J, Cukierman E, Mauck RL, et al. A chemomechanical model of matrix and nuclear rigidity regulation of focal adhesion size. Biophys J 2015;109:1807–17.
20. Lang NR, Skodzek K, Hurst S, Mainka A, Steinwachs J, Schneider J, et al. Biphasic response of cell invasion to matrix stiffness in three-dimensional biopolymer networks. Acta Biomater 2015;13:61–7.
21. Kang JS, Kawakami Y, Bekku Y, Ninomiya Y, Izpisua Belmonte JC, Oohashi T. Molecular cloning and developmental expression of a hyaluronan and proteoglycan link protein gene, crtl1/hapln1, in zebrafish. Zoolog Sci 2008;25:912–8.
22. Wolf K, Mazo I, Leung H, Engelke K, von Andrian UH, Deryugina EI, et al. Compensation mechanism in tumor cell migration: mesenchymal-amoeboid transition after blocking of pericellular proteolysis. J Cell Biol 2003;160:267–77.
23. Park HW. Biological aging and social characteristics: gerontology, the Baltimore city hospitals, and the national institutes of health. J Hist Med Allied Sci 2013;68:49–86.
24. Behera R, Kaur A, Webster MR, Kim S, Ndoye A, Kugel CH 3rd, et al. Inhibition of age-related therapy resistance in melanoma by rosiglitazone-mediated induction of Klotho. Clin Cancer Res 2017; 23:3181–90.
25. Franco-Barraza J, Beacham DA, Amatangelo MD, Cukierman E. Preparation of extracellular matrices produced by cultured and primary fibroblasts. Curr Protoc Cell Biol 2016;71:10.9.1-10.9.34.
26. Franco-Barraza J, Francescone R, Luong T, Shah N, Madhani R, Cukierman G, et al. Matrix-regulated integrin alphavbeta5 maintains alpha5beta1-dependent desmoplastic traits prognostic of neoplastic recurrence. Elife 2017;6.
27. Amatangelo MD, Bassi DE, Klein-Szanto AJ, Cukierman E. Stroma-derived three-dimensional matrices are necessary and sufficient to promote desmoplastic differentiation of normal fibroblasts. Am J Pathol 2005;167:475–88.
28. Papageorgis P, Stylianopoulos T. Role of TGFbeta in regulation of the tumor microenvironment and drug delivery (review). Int J Oncol 2015;46:933–43.
29. Dugina V, Alexandrova A, Chaponnier C, Vasiliev J, Gabbiani G. Rat fibroblasts cultured from various organs exhibit differences in alpha-smooth muscle actin expression, cytoskeletal pattern, and adhesive structure organization. Exp Cell Res 1998;238:481–90.
30. Shenoy VB, Wang H, Wang X. A chemo-mechanical free-energy-based approach to model durotaxis and extracellular stiffness-dependent contraction and polarization of cells. Interface Focus 2016;6:20150067.
31. Provenzano PP, Eliceiri KW, Campbell JM, Inman DR, White JG, Keely PJ. Collagen reorganization at the tumor-stromal interface facilitates local invasion. BMC Med 2006;4:38.

32. Aladowicz E, Ferro L, Vitali GC, Venditti E, Fornasari L, Lanfrancone L. Molecular networks in melanoma invasion and metastasis. Future Oncol 2013;9:713–26.
33. Gaggioli C, Hooper S, Hidalgo-Carcedo C, Grosse R, Marshall JF, Harrington K, et al. Fibroblast-led collective invasion of carcinoma cells with differing roles for RhoGTPases in leading and following cells. Nat Cell Biol 2007;9:1392–400.
34. Bittner M, Meltzer P, Chen Y, Jiang Y, Seftor E, Hendrix M, et al. Molecular classification of cutaneous malignant melanoma by gene expression profiling. Nature 2000;406:536–40.
35. Wolf K, Te Lindert M, Krause M, Alexander S, Te Riet J, Willis AL, et al. Physical limits of cell migration: control by ECM space and nuclear deformation and tuning by proteolysis and traction force. J Cell Biol 2013;201:1069–84.
36. Arencibia I, Sundqvist KG. Collagen receptor on T lymphocytes and the control of lymphocyte motility. Eur J Immunol 1989;19:929–34.
37. Friedl P, Noble PB, Zanker KS. Lymphocyte locomotion in three-dimensional collagen gels. Comparison of three quantitative methods for analysing cell trajectories. J Immunol Methods 1993;165:157–65.
38. Peske JD, Woods AB, Engelhard VH. Chapter eight - control of CD8 T-cell infiltration into tumors by vasculature and microenvironment. Immunother Cancer 2015;128:263–307.
39. Somasundaram R, Robbins P, Moonka D, Loh E, Marincola F, Patel A, et al. CD4(+), HLA class I-restricted, cytolytic T-lymphocyte clone against primary malignant melanoma cells. Int J Cancer 2000;85: 253–9.
40. Goetz JG, Minguet S, Navarro-Lerida I, Lazcano JJ, Samaniego R, Calvo E, et al. Biomechanical remodeling of the microenvironment by stromal caveolin-1 favors tumor invasion and metastasis. Cell 2011;146:148–63.
41. Gehler S, Ponik SM, Riching KM, Keely PJ. Bi-directional signaling: extracellular matrix and integrin regulation of breast tumor progression. Crit Rev Eukaryot Gene Expr 2013;23:139–57.
42. Conklin MW, Eickhoff JC, Riching KM, Pehlke CA, Eliceiri KW, Provenzano PP, et al. Aligned collagen is a prognostic signature for survival in human breast carcinoma. Am J Pathol 2011;178:1221–32.
43. Oudin MJ, Jonas O, Kosciuk T, Broye LC, Guido BC, Wyckoff J, et al. Tumor cell-driven extracellular matrix remodeling drives haptotaxis during metastatic progression. Cancer Discov 2016;6:516–31.
44. Pickup MW, Laklai H, Acerbi I, Owens P, Gorska AE, Chytil A, et al. Stromally derived lysyl oxidase promotes metastasis of transforming growth factor-beta-deficient mouse mammary carcinomas. Cancer Res 2013;73:5336–46.
45. Lo A, Wang LC, Scholler J, Monslow J, Avery D, Newick K, et al. Tumor-promoting desmoplasia is disrupted by depleting FAP-expressing stromal cells. Cancer Res 2015;75:2800–10.
46. Madri JA, Graesser D. Cell migration in the immune system: the evolving inter-related roles of adhesion molecules and proteinases. Dev Immunol 2000;7:103–16.
47. Ivanoff J, Talme T, Sundqvist KG. The role of chemokines and extracellular matrix components in the migration of T lymphocytes into three-dimensional substrata. Immunology 2005;114:53–62.
48. Ferguson AR, Engelhard VH. CD8 T cells activated in distinct lymphoid organs differentially express adhesion proteins and coexpress multiple chemokine receptors. J Immunol 2010;184:4079–86.
49. Cliff JM, Andrade IN, Mistry R, Clayton CL, Lennon MG, Lewis AP, et al. Differential gene expression identifies novel markers of CD4+ and CD8+ T cell activation following stimulation by Mycobacterium tuberculosis. J Immunol 2004;173:485–93.
50. Han XQ, Gong ZJ, Xu SQ, Li X, Wang LK, Wu SM, et al. Advanced glycation end products promote differentiation of CD4(+) T helper cells toward pro-inflammatory response. J Huazhong Univ Sci Technolog Med Sci 2014;34:10–7.
51. Moreau JF, Pradeu T, Grignolio A, Nardini C, Castiglione F, Tieri P, et al. The emerging role of ECM crosslinking in T cell mobility as a hallmark of immunosenescence in humans. Ageing Res Rev 2017;35: 322–35.
52. Sapey E, Greenwood H, Walton G, Mann E, Love A, Aaronson N, et al. Phosphoinositide 3-kinase inhibition restores neutrophil accuracy in the elderly: toward targeted treatments for immunosenescence. Blood 2014;123:239–48.
53. Park CO, Kupper TS. The emerging role of resident memory T cells in protective immunity and inflammatory disease. Nat Med 2015;21: 688–97.
54. Kugel CH 3rd, Douglass SM, Webster MR, Kaur A, Liu Q, Yin X, et al. Age correlates with response to anti-PD1, reflecting age-related differences in intratumoral effector and regulatory T-cell populations. Clin Cancer Res 2018. doi: 10.1158/1078-0432.CCR-18-1116
55. Rasanen K, Sriswasdi S, Valiga A, Tang HY, Zhang G, Perego M, et al. Comparative secretome analysis of epithelial and mesenchymal subpopulations of head and neck squamous cell carcinoma identifies S100A4 as a potential therapeutic target. Mol Cell Proteomics 2013;12:3778–92.
56. Cox J, Mann M. MaxQuant enables high peptide identification rates, individualized p.p.b.-range mass accuracies and proteome-wide protein quantification. Nat Biotechnol 2008;26:1367–72.
57. Li L, Fukunaga-Kalabis M, Herlyn M. The three-dimensional human skin reconstruct model: a tool to study normal skin and melanoma progression. J Vis Exp 2011. pii: 2937
58. Puspoki Z, Storath M, Sage D, Unser M. Transforms and operators for directional bioimage analysis: a survey. Adv Anat Embryol Cell Biol 2016;219:69–93.